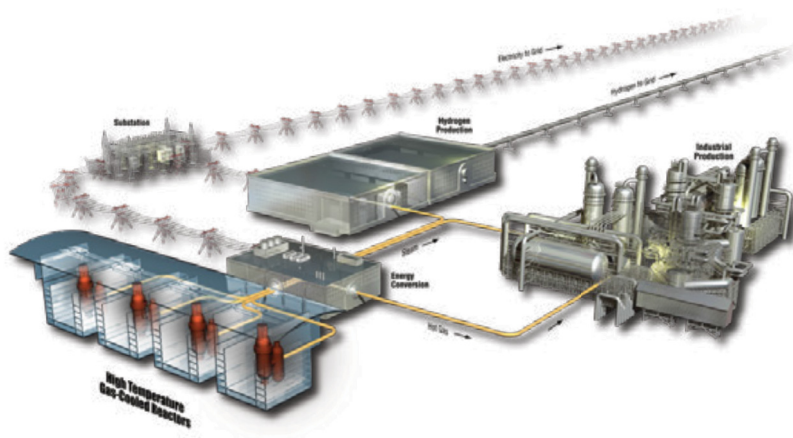


Ceramography of Irradiated TRISO Fuel from the AGR-2 Experiment

F. J. Rice, J. D. Stempien, P. A. Demkowicz

September 2016

The INL is a
U.S. Department of Energy
National Laboratory
operated by
Battelle Energy Alliance



DISCLAIMER

This information was prepared as an account of work sponsored by an agency of the U.S. Government. Neither the U.S. Government nor any agency thereof, nor any of their employees, makes any warranty, expressed or implied, or assumes any legal liability or responsibility for the accuracy, completeness, or usefulness, of any information, apparatus, product, or process disclosed, or represents that its use would not infringe privately owned rights. References herein to any specific commercial product, process, or service by trade name, trade mark, manufacturer, or otherwise, does not necessarily constitute or imply its endorsement, recommendation, or favoring by the U.S. Government or any agency thereof. The views and opinions of authors expressed herein do not necessarily state or reflect those of the U.S. Government or any agency thereof.

Ceramography of Irradiated TRISO Fuel from the AGR-2 Experiment

F. J. Rice, J. D. Stempien, P. A. Demkowicz

September 2016

**Idaho National Laboratory
INL ART TDO Program
Idaho Falls, Idaho 83415**

<http://www.inl.gov>

**Prepared for the
U.S. Department of Energy
Office of Nuclear Energy
Under DOE Idaho Operations Office
Contract DE-AC07-05ID14517**


INL ART TDO Program

Ceramography of Irradiated TRISO Fuel from the AGR-2 Experiment

INL/EXT-16-39462
Revision 0

September 2016

Author:


Francine J. Rice
PIE Engineer

9-27-2016

Date

Approved by:


Paul A. Demkowicz
ART TRISO Fuel Technical Director

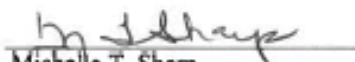
9/27/16

Date


Diane V. Croson
INL ART TDO Deputy Director

9/27/16

Date


Michelle T. Sharp
INL ART TDO Quality Engineer

9/27/16

Date

SUMMARY

Ceramography was performed on cross sections from four tristructural isotropic (TRISO) coated particle fuel compacts taken from the AGR-2 experiment, which was irradiated between June 2010 and October 2013 in the Advanced Test Reactor. The fuel compacts examined in this study contained TRISO-coated particles with either uranium oxide (UO_2) kernels or uranium oxide/uranium carbide (UCO) kernels that were irradiated to final burnups between 9.0 and 11.1% fissions per initial metal atom. These examinations were intended to explore kernel and coating morphology after irradiation. This included analysis of kernel porosity, kernel swelling, and irradiation-induced TRISO coating layer fracture and separation. Variations in behavior within a specific cross section, which could be related to temperature or burnup gradients within the fuel compact, were also explored. The criteria for categorizing post-irradiation particle morphologies, developed for AGR-1 ceramographic exams, were applied to the particles in the AGR-2 compacts examined. AGR-2 results were compared with similar investigations performed as part of the earlier AGR-1 irradiation experiment. This report presents the results of the AGR-2 examinations and discusses the key implications for fuel irradiation performance.

AGR-2 UCO compact cross-sectional surfaces demonstrate that the characterized particles performed in a manner generally consistent with UCO fuel previously analyzed. Data suggest that higher irradiation temperatures may reduce buffer-fracture occurrences. The longer fluidization time between the end of buffer deposition and the start of deposition of the IPyC layer appears to have been successful in facilitating the separation of the buffer from the IPyC during the densification/shrinkage process of the buffer during irradiation. It has thus reduced the occurrence and severity of fractures/tears in the IPyC. Compared to AGR-1 where several through-layer IPyC fractures were observed, no through-layer IPyC fractures were observed in any AGR-2 particles, and only a few IPyC layer tears were observed. Given the reduced occurrence of AGR-2 IPyC fractures compared to AGR-1, and the demonstration of very promising overall performance of the AGR-1 fuel during irradiation and subsequent safety testing, it is expected that AGR-2 fuel will also perform well during safety testing. The results of the present ceramographic study indicate good AGR-2 fuel performance during irradiation, with no significant issues expected in terms of coating failures.

No typical Type B particles (characterized by a completely intact buffer-IPyC interface in the plane observed) were noted in AGR-2 in either the UCO or UO_2 fuel such as those that were observed in AGR-1. The only Type B particle found was a UO_2 particle that was atypical due to a complete debond of the IPyC from the SiC layer (the first such particle observed in either AGR-1 or AGR-2). All layers in this particle were found to be intact in the plane observed.

In AGR-2 UCO fuel, the buffer fracture frequency was found to decrease with increasing irradiation temperature (from 38% fracture at 1080°C to 2% fracture at 1220°C). The limited range of irradiation conditions for fuel compacts in the single AGR-2 UO_2 capsule make determining correlations with temperature, burnup, and fluence challenging for the UO_2 fuel. Data from the single UO_2 fuel compact presented here suggest that buffer fracture and kernel expansion was less likely in the UO_2 fuel than the UCO fuel. The factors contributing to this observed difference are not known at this time, but may include differences in radiation-induced kernel

swelling rates between UO_2 and UCO and the higher burnup of the UCO fuel. Spatial trends for buffer fractures were also noted in the UCO fuel compacts and may be related to temperature gradients within the compact during irradiation.

ACKNOWLEDGEMENTS

The authors wish to acknowledge the highly skilled operators at HFEF that have made this report possible by preparing these AGR-2 specimens for ceramographic examination. These individuals are Brian Frickey, Cassie Anderson and Marc Babcock (sectioning, grinding and polishing). A special thanks goes to Colt Killian and Kelly Williams for the dynamic response to an always-changing schedule for two very busy workstations, our containment box and metallography hot cell.

CONTENTS

SUMMARY	vii
ACKNOWLEDGEMENTS	ix
ACRONYMS	xvi
1. Introduction	1
2. AGR-2 EXPERIMENT BACKGROUND	1
2.1 Fabrication	1
2.2 Irradiation	2
3. SPECIMEN PREPARATION AND ANALYSIS	3
3.1 Sample preparation	3
3.2 Mount analysis	4
3.3 Particle Cataloging	5
4. AGR-2 RESULTS	7
4.1 Fuel Particle Morphological Attributes	7
4.2 Particle Types	9
4.3 Behavior of TRISO Layers	12
4.3.1 Buffer Fractures	12
4.3.2 IPyC Tears	15
4.3.3 SiC and OPyC Observations	17
4.4 Fuel Kernel Observations and Behaviors	18
4.4.1 Qualitative Observations	18
4.4.2 Fuel Kernel Swelling	20
4.4.3 Fuel Kernel Pore Sizes	22
4.5 Particle Type Spatial Distribution	23
5. AGR-2 and AGR-1 UCO PARTICLE COMPARISONS	27
5.1 Particle Types	27
5.2 Buffer Fractures	28
5.3 IPyC Tears	30
6. Conclusions	32
7. REFERENCES	33

FIGURES

Figure 1. Axial schematic of the AGR-2 capsule configurations (left) and cross-sectional schematic of an AGR-2 capsule (right). ⁸	3
--	---

Figure 2. Cutting diagram for AGR-2 compacts, illustrating how bright paint was used to maintain the orientations of the discrete sections for alignment relative to the mount reference markers. Relative to mount IDs from Table 2, 67X would be #1, 68X, #2 and 69X, #3 and so on for each compact.	4
Figure 3. Two micrograph montage examples: (a) Compact 2-1-3, MNT 67X and (b) Compact 3-2-3, MNT 61X for UCO and UO ₂ respectively.	5
Figure 4. Micrograph montage for Compact 2-1-3, MNT 67X, with serial numbers and particle types (PT) assigned to the selected particles.	6
Figure 5. The example AGR-2 particle IDs are: Ai: 213-67X-2 (AGR-2), Af: 213-67X-10 (AGR-2), ABi: 213-67X-23 (AGR-2), ABf: 213-67X-66 (AGR-2). Note that the Bi and Bf examples are AGR-1 particles from Ref. 3 since neither of these types was observed in the AGR-2 particles examined in this study.	8
Figure 6. AGR-2 compact particle type percentages within each compact.	10
Figure 7. AGR-2 compact particle sub-type percentages.	10
Figure 8. Frequency of particle attribute type plotted relative to the fast neutron fluence.	11
Figure 9. Frequency of particle type plotted relative to the TAVA irradiation temperature.	11
Figure 10. Particle 323-61X-34 from UO ₂ Compact 3-2-3 showing the only Type B, specifically Bi, characteristic. Note the IPyC debond from the SiC.	12
Figure 12. UO ₂ particle 323-62X-26 with Type ABf characteristics showing two radial cracks in the buffer propagating from a gap filled with epoxy between the kernel and the buffer layer.	13
Figure 13. Buffer fracture percent for AGR-2 UCO and UO ₂ . UCO Compact 2-1-3, comparable in TAVA temperature to the UO ₂ Compact 3-2-3, is called out specifically.	14
Figure 14. Buffer fracture frequencies relative to TAVA temperature.	14
Figure 15. Buffer fracture frequencies relative to fast neutron fluence (E>0.18 MeV).	15
Figure 16. AGR-2 fuel particle IPyC tear examples. Particles shown are 213-68X-20 (left) and 213-69X-28 (right).	16
Figure 17. An example of an Ai particle (243-58X-57) with a buffer strip still attached to the IPyC at a tear location.	17
Figure 18. Particle 323-63X-3 with Type Ai characteristics showing the typical UO ₂ fuel kernel morphology with the buffer intact with small strips of buffer adhered to the IPyC.	17
Figure 19. UCO Particle 213-68X-1 showing the carbide skin.	18
Figure 20. UO ₂ Particle 323-61X-13 showing a thin halo at the kernel-buffer that appears to have reduced porosity.	19
Figure 21. UCO particle 213-69X-6 showing fuel kernel crack.	19
Figure 22. Particle 323-63X-7 with a fuel kernel crack.	20
Figure 23. Particle 513-65X-53 with Type Ai characteristics showing the typical UCO fuel-kernel morphology, intact buffer, and complete buffer-IPyC debonding.	20
Figure 24. Particle 513-65X-4 with Type Af characteristics showing the typical UCO fuel-kernel morphology with the buffer fractured in several locations.	21

Figure 25. At left, Particle 323-63X-5 (Type ABf) showing the typical UO ₂ fuel kernel morphology with two narrow, radial buffer cracks. At right, Particle 323-62X-27 (Type Af) with a single through-layer radial buffer crack and a partial crack.	21
Figure 26. Particle 243-60X-16 with Type Ai characteristics showing the typical UCO fuel-kernel pore morphology when the buffer remained intact.	22
Figure 27. Particle 323-61X-32 with Type ABi characteristics showing a typical UO ₂ fuel-kernel porosity distribution.	23
Figure 28. Compact 2-1-3 grayscale particle types showing evidence of a buffer failure gradient likely due to a temperature gradient within the compact. Relative to the cutting diagram (Figure 2), MNT 69X is piece #2, MNT 67X is piece #1 and MNT 68X is piece #3.	24
Figure 29. Compact 2-4-3 grayscale particle types. Relative to the cutting diagram (Figure 2), MNT 60X is piece #2, MNT 58X is piece #1 and MNT 59X is piece #3.	25
Figure 32. Comparison of UCO particle sub-types between AGR-2 and AGR-1.	28
Figure 33. Buffer fracture frequency relative to particle attribute type. Recall that 5% of AGR-1 particles were type Bi particles.	29
Figure 34. Percentage of particles with fractured buffers for AGR-2 and AGR-1 UCO compacts.	29
Figure 35. AGR-1 particle 213-138T-55 (left) and AGR-2 particle 513-65X-9 (right).	30
Figure 36. (a.) AGR-1 Particle 333-56T-50 showing multiple IPyC fractures with two associated with buffer fractures. (b.) AGR-2 Particle 213-69X-28 showing the most severe IPyC tear observed in the AGR-2 compact cross sections.	31
Figure 37. Comparison of the percentages of each particle type that exhibited IPyC tears for AGR-1 (through and partial tears are shown separately) and AGR-2.	32
Figure A-1. UCO Compact 2-1-3 center, MNT 67X micrograph montage.	36
Figure A-2. UCO Compact 2-1-3 top, MNT 69X micrograph montage.	37
Figure A-3. UCO Compact 2-1-3 bottom, MNT 68X micrograph montage.	38
Figure A-4. UCO Compact 2-4-3 middle, MNT 58X micrograph montage.	39
Figure A-5. UCO Compact 2-4-3 top, MNT 60X micrograph montage.	40
Figure A-6. UCO Compact 2-4-3 bottom, MNT 59X micrograph montage.	41
Figure A-7. UO ₂ Compact 3-2-3 middle, MNT 61X micrograph montage.	42
Figure A-8. UO ₂ Compact 3-2-3 top, MNT 63X micrograph montage.	43
Figure A-9. UO ₂ Compact 3-2-3 bottom, MNT 62X micrograph montage.	44
Figure A-10. UCO Compact 5-1-3 middle, MNT 64X micrograph montage.	45
Figure A-11. UCO Compact 5-1-3 top, MNT 66X micrograph montage.	46
Figure A-12. UCO Compact 5-1-3 bottom, MNT 65X micrograph montage.	47

TABLES

Table 1. Irradiation conditions ⁸ for the AGR-2 compacts selected for ceramography.	2
---	---

ACRONYMS

AGR	Advanced Gas Reactor
BWXT	BWX Technologies
CEA	Commissariat à l'Énergie Atomique
FIMA	fissions per initial metal atom
ID	identification
IPyC	inner pyrolytic carbon
MET	metallography
PBMR	Pebble Bed Modular Reactor Limited
PIE	post-irradiation examinations
PT	particle type
SiC	silicon carbide
TAVA	time average volume average
TRISO	tristructural isotropic
UCO	uranium carbide
UO ₂	uranium oxide

Ceramography of Irradiated TRISO Fuel from the AGR-2 Experiment

1. Introduction

The Advanced Gas Reactor (AGR)-2 experiment, the second in a series of test irradiations for the AGR Fuel Development and Qualification Program¹ contained both uranium oxide (UO₂) and uranium oxide/uranium carbide (UCO) tristructural isotropic (TRISO)-coated particle fuel. The experiment was implemented with the following three objectives²:

1. Irradiate UCO and UO₂ fuel produced in a large (150 mm diameter) coater in an engineering-scale pilot line.
2. Provide irradiated fuel samples for post-irradiation examination and safety testing.
3. Support the development of an understanding of the relationship between fuel-fabrication processes, fuel-product properties, and irradiation performance.

The purpose of performing ceramographic post-irradiation examinations (PIE) on AGR-2 compacts is to provide fuel-performance data to help fulfill Objective 3 of the AGR-2 experiment. Specifically, this was to assess the kernel and coating morphological evolution after irradiation. This includes kernel swelling, kernel porosity and coating fracture. Preparation of fuel compact cross sections enabled particles to be examined in their original locations within the fuel compacts. In this manner, any trends in particle behavior relative to location in the compact, which may have been influenced by local gradients in burnup and temperature, could be identified. Similar examinations were performed previously on fuel from the AGR-1 irradiation experiment,³ and AGR-1 results were compared with the AGR-2 results presented here.

2. AGR-2 EXPERIMENT BACKGROUND

2.1 Fabrication

The UCO and UO₂ fuel kernels were fabricated by BWX Technologies (BWXT). The UCO kernels had mean diameter of 427 μm and ²³⁵U enrichment of 14.0%. The UO₂ kernels had mean diameter of 508 μm and ²³⁵U enrichment of 9.6%. The kernels were coated at BWXT in a 150-mm, engineering-scale coater, representing an important step towards the establishment of industrial-scale fuel fabrication capability for the AGR program. The average coated particle diameters were 873 and 953 μm for UCO and UO₂, respectively. The fabrication parameters used to apply TRISO coatings to both types of kernels were based on the parameters used earlier for the AGR-1 Variant 3 fuel. In Variant 3-type fuel, the SiC layer was deposited at lower temperatures in an argon-hydrogen mixture, which produced a finer grain structure and was expected to reduce SiC defects caused by uranium dispersion.^{4, 5}

One notable difference in the AGR-2 particle coating process relative to AGR-1 was the use of a longer fluidization time between buffer deposition and deposition of the IPyC layer. Post-irradiation examination of the AGR-1 fuel has indicated that a strong buffer-IPyC interfacial bond was implicated in occasional fracture of the IPyC layer. While infrequent, these IPyC fractures appear to be a precursor to subsequent SiC failure by focused attack of fission products.⁶ It is believed that the longer fluidization time used in the AGR-2 particle fabrication may smooth the buffer surface prior to IPyC deposition, and reduce the strength of the bond between the buffer and the IPyC. This could, in turn, promote desirable buffer-IPyC debonding during irradiation and reduce the frequency of IPyC fracture.

The AGR-2 fuel compacts were fabricated at Oak Ridge National Laboratory⁷ using the particles fabricated at BWXT. Overcoated particles were pressed into right cylindrical compacts that were nominally 25.1 mm long and 12.3 mm in diameter. There were an average of 3176 and 1543 particles in the UCO and UO₂ compacts, respectively, resulting in particle volume packing fractions of 37% (UCO)

and 23% (UO₂). Additional details and references for the AGR-2 fuel particles and compacts have been summarized in Collin 2011.²

2.2 Irradiation

The AGR-2 experiment was irradiated in the B-12 position of the Advanced Test Reactor at Idaho National Laboratory and contained six independently controlled and monitored capsules. Capsules 2, 3, 5, and 6 contained fuel fabricated in the US, while the remaining two capsules contained fuel supplied by Commissariat à l'Énergie Atomique (CEA, France) and Pebble Bed Modular Reactor Limited (PBMRL, South Africa). Each US capsule contained 12 fuel compacts of a single type (UO₂ or UCO), arranged in three stacks, each containing four compacts. Test assembly and capsule schematics are shown in Figure 1. Compacts are identified with a numbering scheme based on their location in each capsule during irradiation.² This experiment was irradiated for 559.2 effective full-power days. Selected irradiation conditions for the four compacts analyzed in this report are summarized in

Table 1. Additional details for irradiation conditions are found in INL/EXT-14-32277, “AGR-2 Irradiation Test Final As-Run Report”.⁵

AGR-2 Capsule 2 contained fuel compacts that were irradiated at a significantly elevated temperature relative to the other capsules (time-average peak temperatures were >1300°C for all Capsule 2 compacts), and these higher irradiation temperatures constitute a margin test of TRISO fuel irradiation performance. Capsule 5 had the next-highest capsule-average time-average peak temperature of 1210°C. Capsule 3, with UO₂ fuel, had a capsule-average time-average peak temperature of 1105°C.⁵

Table 1. Irradiation conditions⁵ for the AGR-2 compacts selected for ceramography.

Compact	Capsule	Fuel Type	TA Min ^a temperature (°C)	TAVA ^b temperature (°C)	TA Max ^c temperature (°C)	Average burnup (% FIMA)	Average fast fluence (× 10 ²⁵ n/m ² , E>0.18 MeV)
2-1-3	2	UCO	1034	1194	1305	10.95	2.88
2-4-3	2	UCO	1054	1216	1324	11.52	3.08
3-2-3	3	UO ₂	980	1045	1092	9.01	3.09
5-1-3	5	UCO	936	1078	1177	11.09	3.03

- a. Time-average minimum
- b. Time-average volume-average
- c. Time-average maximum

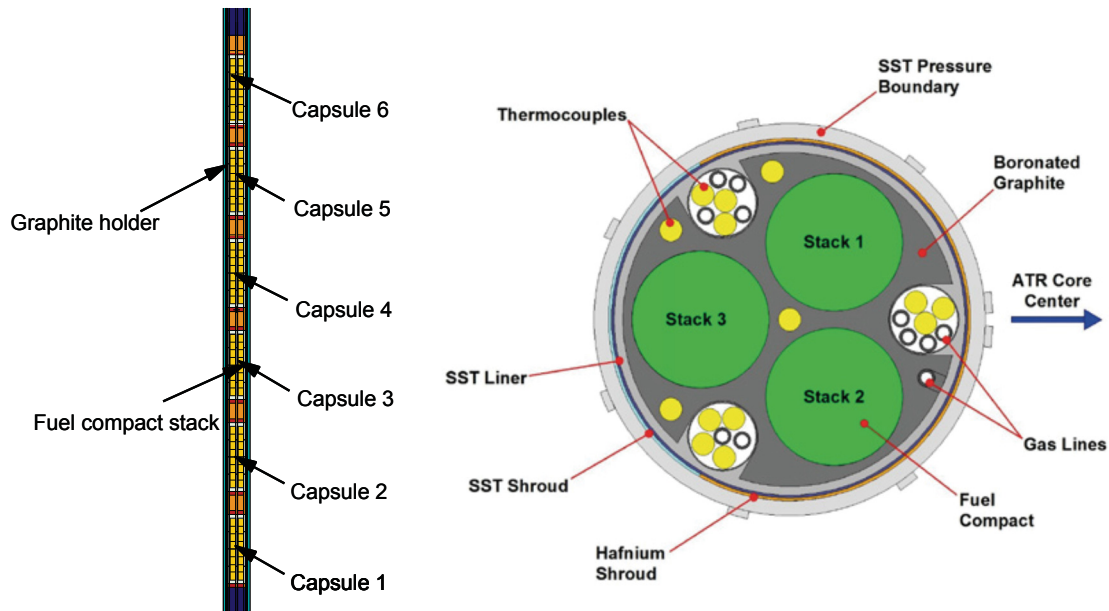


Figure 1. Axial schematic of the AGR-2 capsule configurations (left) and cross-sectional schematic of an AGR-2 capsule (right).⁵

3. SPECIMEN PREPARATION AND ANALYSIS

3.1 Sample preparation

In light of the objectives outlined in Section 1, four AGR-2 compacts (listed in

Table 1) with different kernel types and/or irradiation histories were selected for ceramographic examination and comparison. Methods applied for the specimen preparation and examination were those developed during the AGR-1 ceramography campaign and can be found in INL/EXT-12-25301 Revision 1 “Ceramographic Examinations of Irradiated AGR-1 Fuel Compacts”. A brief summary of the steps to track compact segments, mount the segments in epoxy, remove regions with damage and particle pullout, and achieve the final polish is given below.

- Compacts were sectioned along dashed lines shown in Figure 2 using a low-speed saw and each section was labeled as indicated in Figure 2. Note that the axial orientation (i.e., top and bottom) of the compact relative to its position in the irradiation capsule was maintained during PIE, but the azimuthal orientation of the compact in the capsule was not known following capsule disassembly.
- Each of the numbered cross sections in Figure 2 was placed into a Micarta mount with orientation relative to the paint.
- Each cross section was potted using Buehler Epoheat[®] epoxy aided with vacuum impregnation prior to heat curing.
- Each metallography (“met”) mount was ground using 220-grit, then 500-grit Struers MD-Piano[®] grinding discs, and then 1200-grit Struers MD-Piano[®] grinding discs to remove the very thick layer of epoxy covering the mount and to remove the layer with saw damage. A back-pot (a very thin addition of epoxy lightly brushed on with a cotton swab to the ground mount surface) was applied between each grit-coarseness reduction using a thin layer of Buehler Epoheat[®] epoxy aided with vacuum impregnation prior to heat curing. This helped

retain particles as well as kernel and coating fragments in the mount during grinding using the finer grits and during the follow-on polishing. The objective was to grind sufficiently beyond the initial region of saw damage, thus revealing particles with minimal sample processing damage. Each mount was carefully examined periodically through the hot-cell periscope during preparation to monitor loss of further particles and to anticipate regions likely to lose particles.

- Once the epoxy from the initial potting of the specimen was removed, in-process mount thickness measurements were performed to monitor material removal. This provided a means to determine when a thickness approximately equal to a particle radius had been removed, thus revealing fresh particles without saw damage and a minimal number of void spaces in locations where a particle had been pulled out by sample-preparation forces.
- Once grinding had removed the desired amount of material, all mounts were polished starting with a 3 micron disc and working down to 1 micron. Visual exams of the progress were made via the hot cell periscope. Final inspection of the surface-finish quality was performed after transferring the mounts to the microscope.

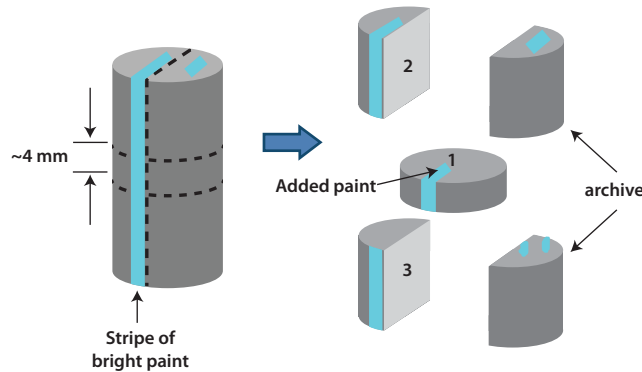


Figure 2. Cutting diagram for AGR-2 compacts, illustrating how bright paint was used to maintain the orientations of the discrete sections for alignment relative to the mount reference markers. Relative to mount IDs from Table 2, 67X would be #1, 68X, #2 and 69X, #3 and so on for each compact.

The total amount of material removed from each cross section was estimated to be approximately half a particle diameter (approximately 400-500 μm). It was determined that most of the particles that were lost during the sectioning activity were lost due to encountering the saw blade at (or below) roughly mid-plane of the particle diameter, which elevates the risk of particle loss. In-process observations through the periscope revealed that all but a few compact cross sections had additional particle losses during the grinding and polishing activity, and of those few, only 1–3 particles were lost.

3.2 Mount analysis

Each mount was optically examined using an in-cell Leitz metallograph coupled with a 6.6-megapixel Leaf Volare camera located out-of-cell to capture the projected images. A series of micrographs were collected using a 50X objective while traversing back and forth across the entire mount surface. The micrographs were merged together using Photoshop[®] software to create a montage of each mount. Since the microscope lighting is not perfectly uniform, montages may have a tiled appearance. However this did not interfere with the analysis of the mount montages.

Once each montage was created, each particle was examined for indication of an exposed fuel kernel and assigned a serial number. Examples of UCO and UO_2 micrograph montages are shown in Figure 3.

All 50X compact section montages can be found in Appendix A. A single 100X magnification micrograph was collected for each particle that was a candidate for characterization and categorization according to its morphology (morphology criteria are explained in Section 4). Selected particles with interesting features such as excessive buffer cracking and kernel expansion were examined using a 200X magnification. This required collecting several micrographs and subsequently merging them to create a particle montage.

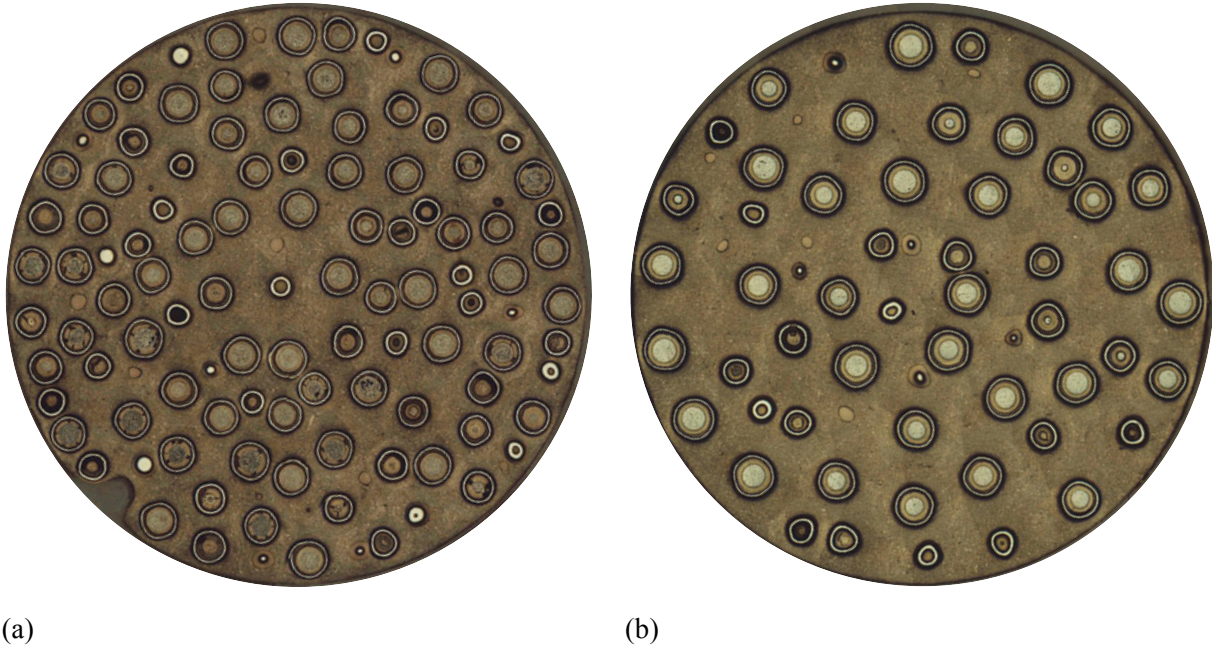


Figure 3. Two micrograph montage examples: (a) Compact 2-1-3, MNT 67X and (b) Compact 3-2-3, MNT 61X for UCO and UO_2 respectively.

3.3 Particle Cataloging

Table 2 summarizes the selected compacts and the corresponding ceramography mount identifications. Particles on each polished surface received a unique serial number (numbering convention summarized in Table 3), which was applied according to the processing histories (compact number, met mount, and particle number within the met mount). In the met mount ID, the third character 'X' is a part of the alphanumeric sample tracking system. A particle was selected for characterization only if the fuel kernel was exposed. Additionally, if a candidate particle was located on a cut edge of the compact cross section, it was characterized only if the entire buffer circumference and thickness were intact such that the particle characterization criteria could be determined. Individual micrographs of every particle that could be characterized were collected. Each particle micrograph was labeled with the serial number. The montages comprised of partial-mount micrographs (an example of which is shown in Figure 4) contain the serial numbers for each particle characterized such that the relative position of each particle can be easily determined.

Table 2. Compact characteristics and ceramography mount identifications (the middle mount identification [ID] is the middle disc, the other two are the axial halves from top and bottom of compact).

AGR-2 Compact IDs	Ceramography Cross-section Mount IDs	Fuel Type
2-1-3	69X/67X/68X	UCO
2-4-3	60X/58X/59X	UCO
3-2-3	63X/61X/62X	UO ₂
5-1-3	66X/64X/65X	UCO

Table 3. Particle serial number assignment protocol.

Compact Identification ($X_1X_2X_3$)		
Capsule Number	Axial Compact Position	Radial Compact Stack Position
X_1	X_2	X_3
Particle Serial Number ($X_1X_2X_3$ - X_4X_5X - X_6)		
Compact Identification	Met Mount Identifier	Particle Number
$X_1X_2X_3$	X_4X_5X	X_6

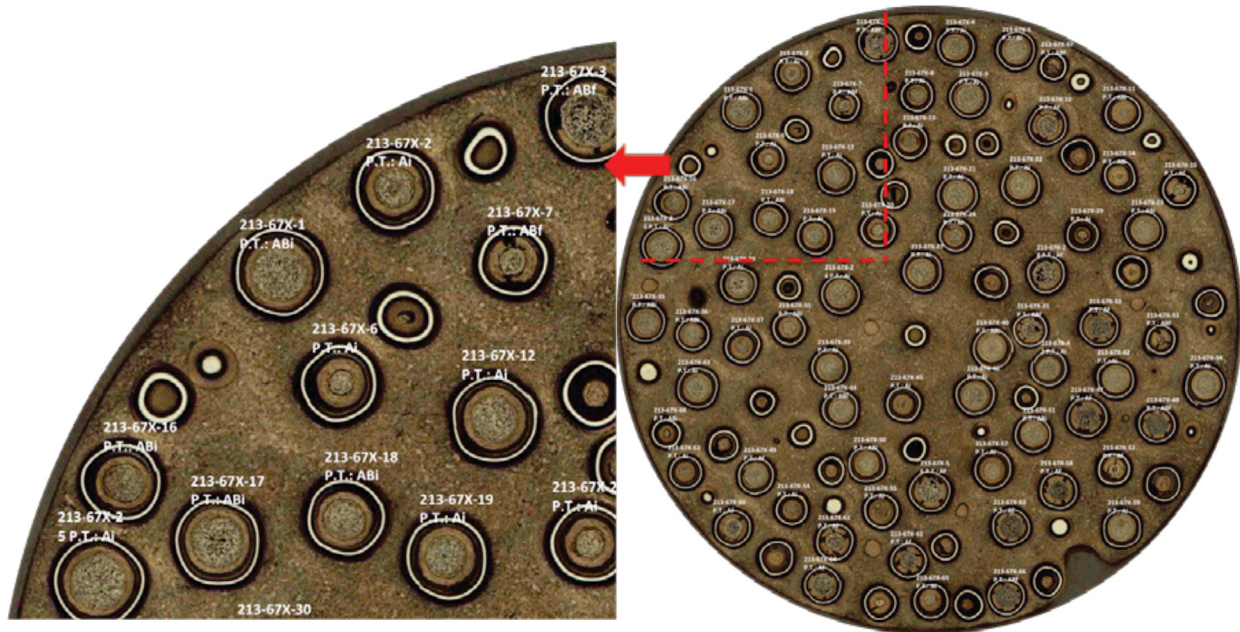


Figure 4. Micrograph montage for Compact 2-1-3, MNT 67X, with serial numbers and particle types (PT) assigned to the selected particles.

4. AGR-2 RESULTS

4.1 Fuel Particle Morphological Attributes

The irradiated particles exhibited several common behaviors, including kernel swelling, pore formation and buffer densification, almost always leading to a gap between the buffer and the inner pyrolytic carbon (IPyC) layer. This gap was either continuous (i.e., complete separation in the plane examined) or partial. In some instances the buffer layer fractured. A total of 640 particles (an average of 178 per UCO compact and 102 per UO₂ compact) were characterized according to the behavior of buffer and IPyC layers using a procedure similar to that in Reference 3. Specifically, the categories are based on (a) whether the buffer and IPyC layers remained bonded or delaminated and (b) whether the buffer layer fractured. Table 4 summarizes the attributes for each major particle type from Reference 3, and Figure 5 shows examples of each type of particle morphology. As discussed further below, no Type B particles representative of those observed previously in the AGR-1 PIE were found in the AGR-2 compact cross sections; therefore, the Type Bi and Bf particles in Figure 5 are examples taken from the AGR-1 work (Reference 3).

Table 4. Post-irradiation characteristic fuel particle attributes³.

Particle Morphology Category	Subcategory (<i>i</i>: intact buffer; <i>f</i>: fractured buffer): Buffer Attributes and IPyC interactions	Fuel Kernel Attribute
A : Complete circumferential buffer-IPyC debond.	Ai : Buffer densification radially inward and intact	Swelling constrained
	Af : Buffer densification inward and fractured	Protrusion into cavities, usually enlarged pores
AB : Partially intact buffer-IPyC bond. Some IPyC fractures	ABi : Buffer densification inward and intact with localized bonding to IPyC	Swelling constrained
	ABf : Buffer densification inward with fractures in non-bonded regions	Protrusion into fracture cavities
B : Fully intact buffer-IPyC bond.	Bi : Buffer densification outward and intact	Larger pores and increased swelling relative to Ai particles.
	Bf : Buffer outward densification and fracture through buffer and IPyC	N/A

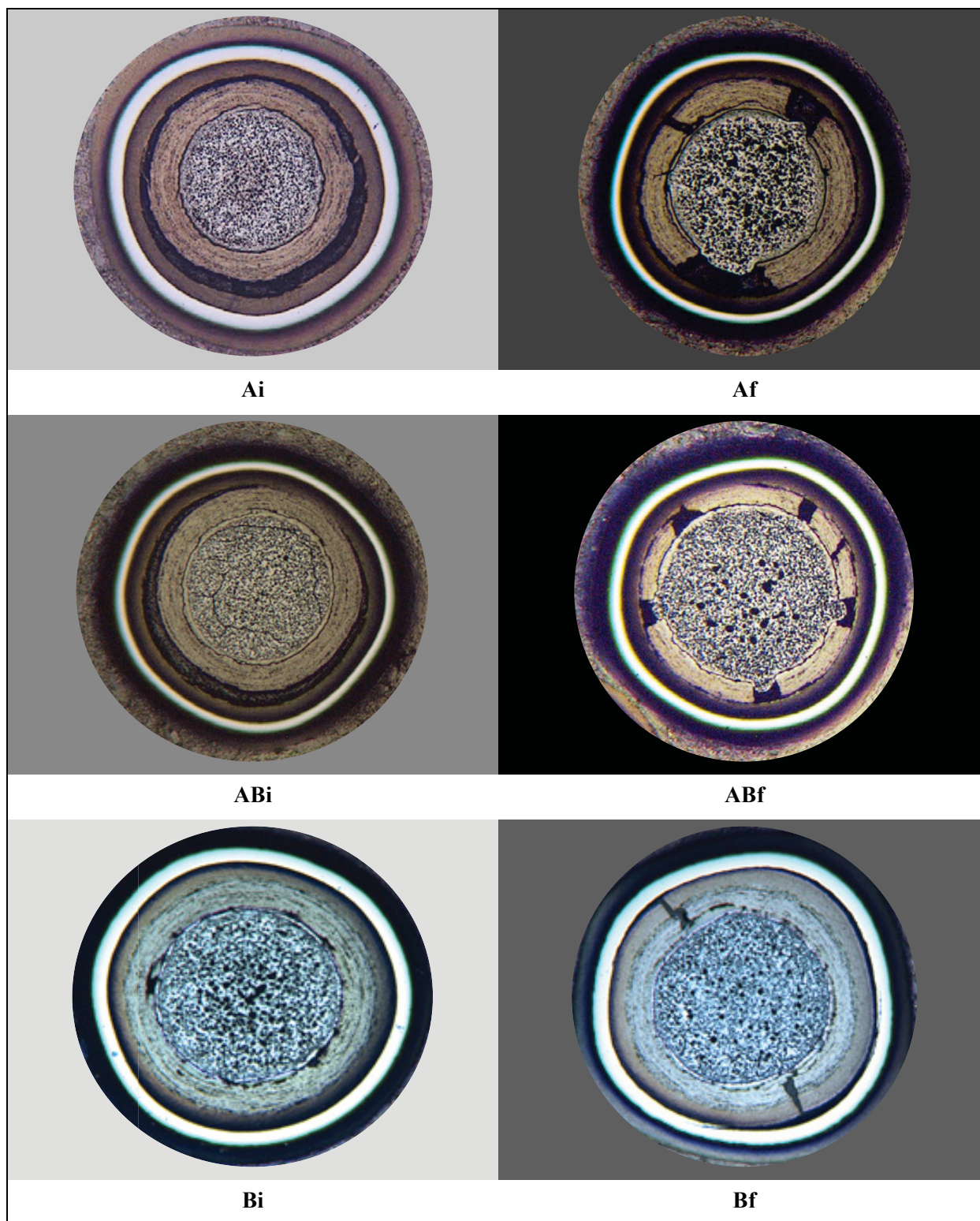


Figure 5. The example AGR-2 particle IDs are: Ai: 213-67X-2 (AGR-2), Af: 213-67X-10 (AGR-2), ABi: 213-67X-23 (AGR-2), ABf: 213-67X-66 (AGR-2). Note that the Bi and Bf examples are AGR-1 particles from Ref. 3 since neither of these types was observed in the AGR-2 particles examined in this study.

Extensive PIE on AGR-1 particles^{3, 8} demonstrated the limitations of the categorization scheme that is based on analysis of particle cross sections in a single plane. Specifically, it was recognized that many particles identified as Type A (complete buffer-IPyC delamination in the polished plane) based on the plane analyzed, may in fact be Type AB particles (partial delamination), because the buffer and IPyC layers are bonded at a location that is not exposed in the micrograph (i.e., below or above the plane of examination). A previous AGR-1 study showed that when multiple planes of polish were observed, the fraction of particles categorized as Type A decreased and the fraction of Type AB particles increased; moreover, the likelihood of observing buffer fractures increased slightly.⁹ Nonetheless, the categorization method remains a useful tool for evaluating the particle morphologies and comparing AGR-2 particle behavior to that observed previously in the AGR-1 particles.

4.2 Particle Types

A summary of the particle types identified in the AGR-2 cross sections is given in Table 5. Note that particle types are also reported as an aggregate for all AGR-2 UCO compacts characterized. Although the frequencies of particle types in the UO₂ compact are generally similar to the UCO compacts, UO₂ fuel has lower burnup, was irradiated at a lower average temperature, and has different kernel chemistry compared to UCO. Data are plotted in Figure 6 and Figure 7, showing the percentage of particles with a particular morphology relative to the totals per compact for particle types and sub-types respectively. The data indicate that there were only small differences in the fraction of major particle types between the four compacts analyzed, but significant differences exist in the (“i” and “f”) sub-types, indicating differences in the relative frequency of buffer fracture. The majority of particles were Type A (complete buffer-IPyC debonding). A single Type B particle was observed in one of the Compact 3-2-3 cross sections, and is discussed further below.

Particle-type frequencies are plotted versus fast fluence ($E > 0.18$ MeV) and time-average volume-average (TAVA) irradiation temperature in Figure 8 and Figure 9, respectively. The data points corresponding to UO₂ particles are highlighted with a gray halo. All other points in the plots are for UCO particles. In Figure 9, there are a few apparent trends in particle type frequencies with TAVA irradiation temperature. In the UCO particles, the frequency of particles with buffer fractures (types Af and ABf) decreases with increasing TAVA irradiation temperature, and the frequency of particles with intact buffers (type Ai particles) increases with increasing TAVA irradiation temperature. This apparent temperature-dependent behavior of the buffer is discussed further in Section 4.3.1. In Figure 8, there are no apparent trends in particle type frequency with fluence. However, note that the range of fluences examined in this study is relatively small (there is only a 7% relative difference between the minimum and maximum compact-average fluence values); therefore, the sample set is not well suited for examining the effect of fluence on particle morphology.

Table 5. Number/percentage of particles types in each of the four selected AGR-2 fuel compacts and the summarized totals for AGR-2.

Compact Identification	Type A		Type B		Type AB		Compact Total Particles
	Ai / percent	Af / percent	Bi / percent	Bf / percent	ABi / percent	ABf / percent	
2-1-3 (UCO)	94 / 47	28 / 14	0 / 0	0 / 0	67 / 34	9 / 5	198
2-4-3 (UCO)	94 / 59	3 / 2	0 / 0	0 / 0	62 / 39	0 / 0	159
3-2-3 (UO ₂)	56 / 55	1 / 1	1 / 1	0 / 0	42 / 41	2 / 2	102
5-1-3 (UCO)	61 / 34	44 / 24	0 / 0	0 / 0	50 / 28	26 / 14	181
AGR-2 UCO Totals	249 / 46	75 / 14	0 / 0	0 / 0	179 / 33	35 / 7	538

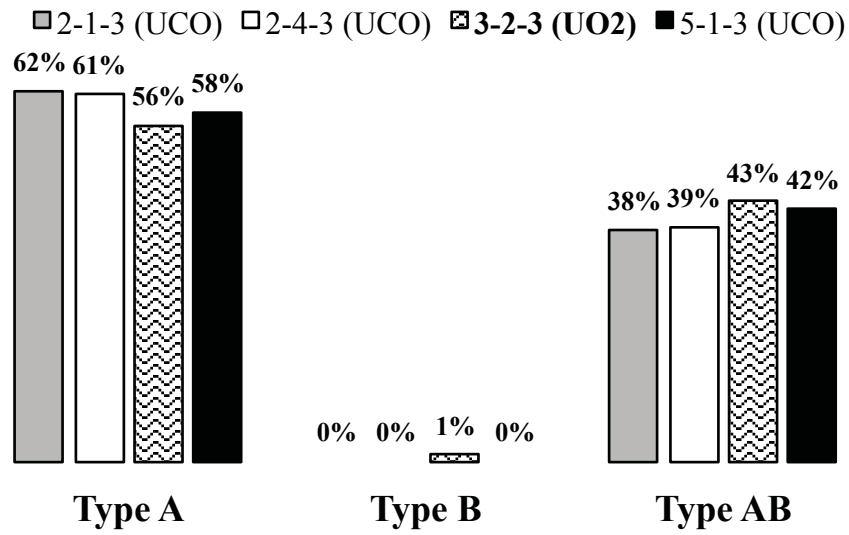


Figure 6. AGR-2 compact particle type percentages within each compact.

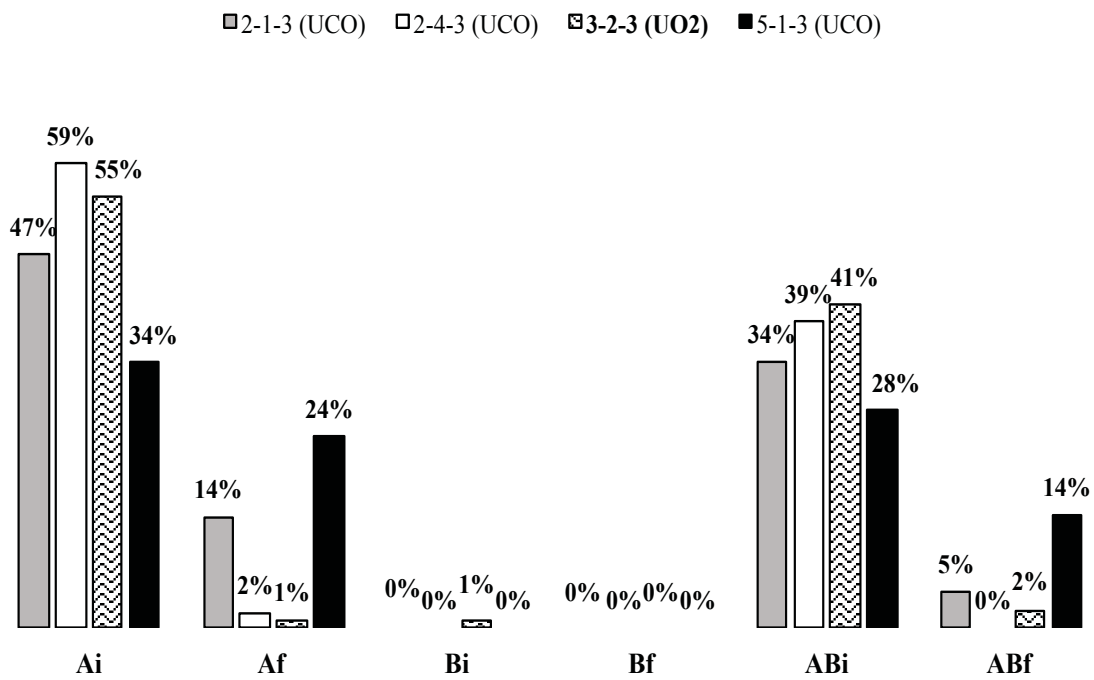


Figure 7. AGR-2 compact particle sub-type percentages.

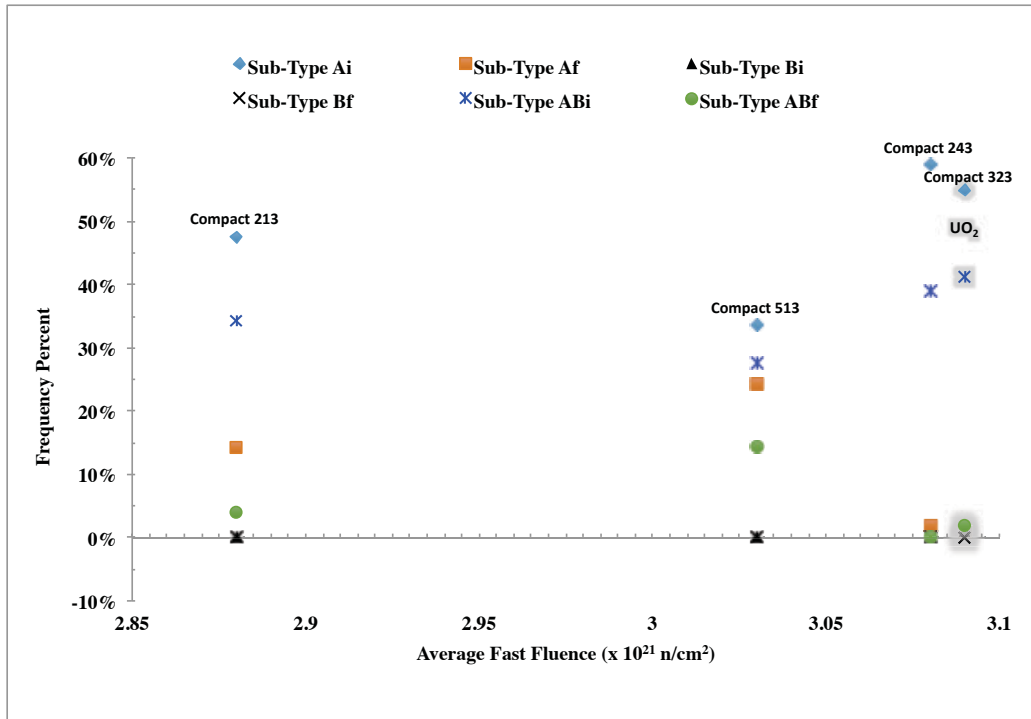


Figure 8. Frequency of particle attribute type plotted relative to the fast neutron fluence.

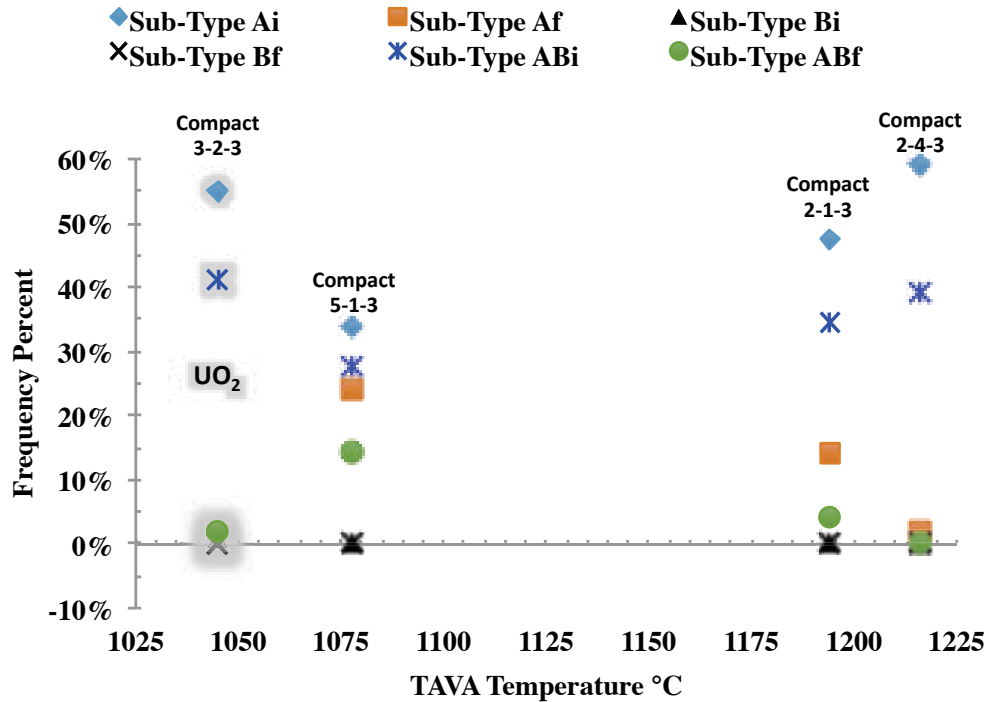


Figure 9. Frequency of particle type plotted relative to the TAVA irradiation temperature.

The only Type B particle noted in the characterized AGR-2 compact cross sections was found in UO₂ Compact 3-2-3, shown in Figure 10. This particle is atypical because while it is technically a Bi subtype,

(where the buffer remained intact and attached to the IPyC), there is also a complete debond of the IPyC from the SiC layer, which may indicate a weak bond between the IPyC and SiC and inward densification of the IPyC (and possibly the buffer as well). Extensive IPyC-SiC debonding of this nature, with fully intact buffer and IPyC, has never been observed previously in AGR-1 or AGR-2 particles either in cross section or in nondestructive three-dimensional analysis of particles using x-ray imaging. It is apparent that while the buffer was densifying, instead of pulling away from the IPyC layer in the conventional manner, the IPyC layer debonded from the SiC, leaving a gap between the IPyC and SiC layers, rather than the normal gap observed between the buffer and IPyC layers. It is also possible that this particle experienced buffer and/or IPyC fracture above or below the plane of polish, and the IPyC fracture could have initiated the IPyC-SiC debonding.

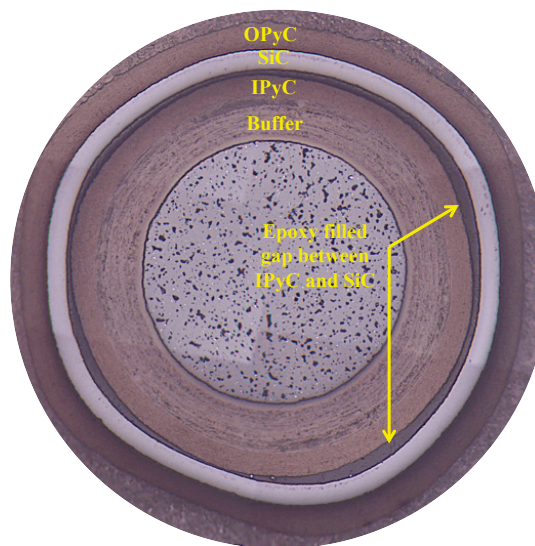


Figure 10. Particle 323-61X-34 from UO₂ Compact 3-2-3 showing the only Type B, specifically Bi, characteristic. Note the IPyC debond from the SiC.

4.3 Behavior of TRISO Layers

4.3.1 Buffer Fractures

Figure 11 and Figure 12 are examples of buffer fractures in UCO and UO₂ particles, respectively. In Figure 11, there are four radial cracks in the buffer layer, and the kernel has expanded into two of these cracks. In AGR-2 UCO particles with buffer cracks, the buffers typically contained four or more radial cracks. Figure 12 shows a UO₂ particle with two narrow radial cracks that propagate from the fuel kernel-buffer interface. Buffer cracks in UO₂ particles were much narrower than in UCO particles, and UO₂ kernel expansion into these narrow buffer cracks was not observed. Additional discussion of kernel expansion (and buffer cracking) is given in Section 4.4.2.

Figure 13 compares buffer fracture frequencies of UCO fuel with UO₂. Total buffer fracture for AGR-2 UCO fuel is 20%, compared to 3% for the UO₂ particles characterized. However, the ability to explore temperature, burnup, and fluence effects in the UO₂ fuel was limited since the range of these parameters for the 12 UO₂ fuel compacts in Capsule 3 was very narrow.⁵ Nevertheless, comparing the buffer fracture frequencies in Figure 13 suggests that the incidence of buffer fracture is generally lower in this UO₂ fuel than in the UCO fuel. Recall that the burnup of the UO₂ compact was about 2% FIMA lower than that of the UCO compacts examined in this study; however, UO₂ Compact 3-2-3, and UCO Compact 2-1-3 (called out separately in Figure 13) both had similar TAVA irradiation temperatures. The percentages of buffer fractures in each compact relative to TAVA temperature and fluence are shown in Figure 14 and

Figure 15, respectively. For the UCO fuel, Figure 14 indicates an inverse correlation of buffer fractures with temperature, with fewer incidences of buffer fracture at higher temperatures. Preliminary data from microscopic analysis of loose particles from other AGR-2 compacts supports this general trend.¹⁰ It is believed that this lower incidence of buffer fracture at higher temperatures is related to increased thermal creep in the layer, enabling stresses from radiation-induced shrinkage to be more readily relaxed. A buffer fracture correlation with fluence is not evident in Figure 15.

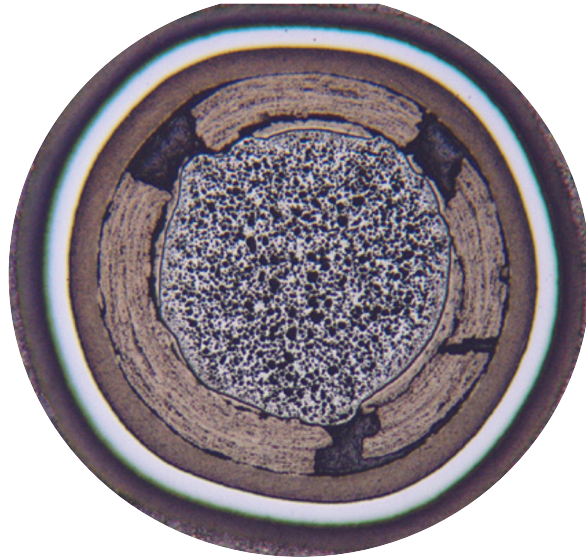


Figure 11. Radial buffer cracks and kernel expansion into the buffer cracks in Particle 213-67X-32

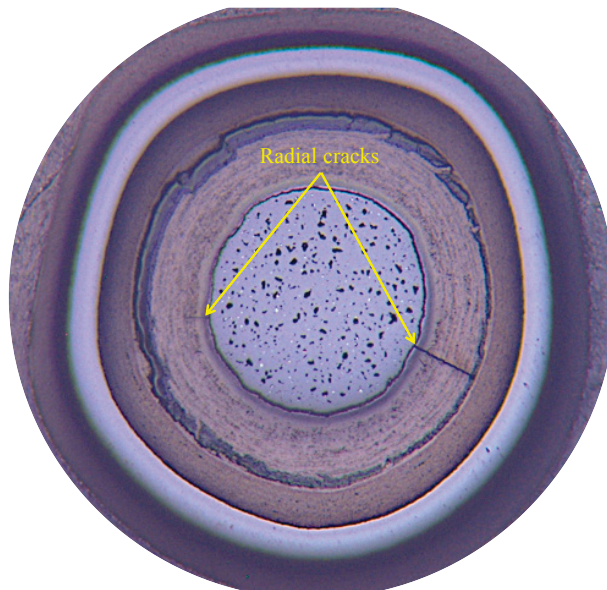


Figure 12. UO_2 particle 323-62X-27 with Type Af characteristics showing two radial cracks in the buffer with both propagating from the fuel kernel-buffer interface.

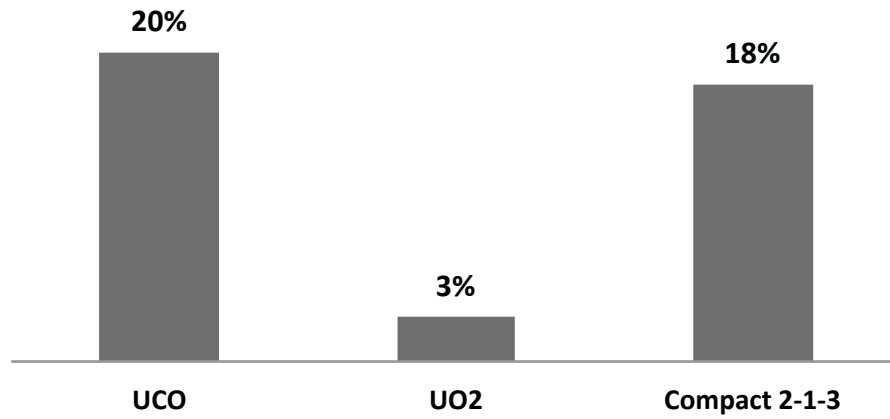


Figure 13. Buffer fracture percent for AGR-2 UCO and UO₂. UCO Compact 2-1-3, comparable in TAVA temperature to the UO₂ Compact 3-2-3, is called out specifically.

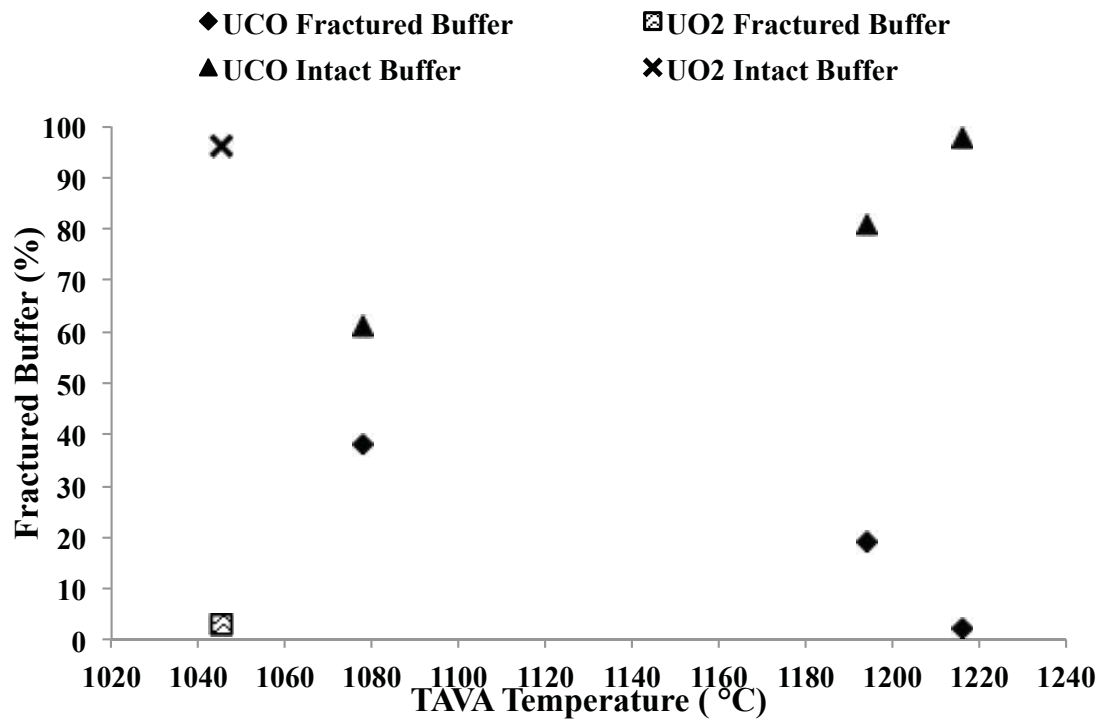


Figure 14. Buffer fracture frequencies relative to TAVA temperature.

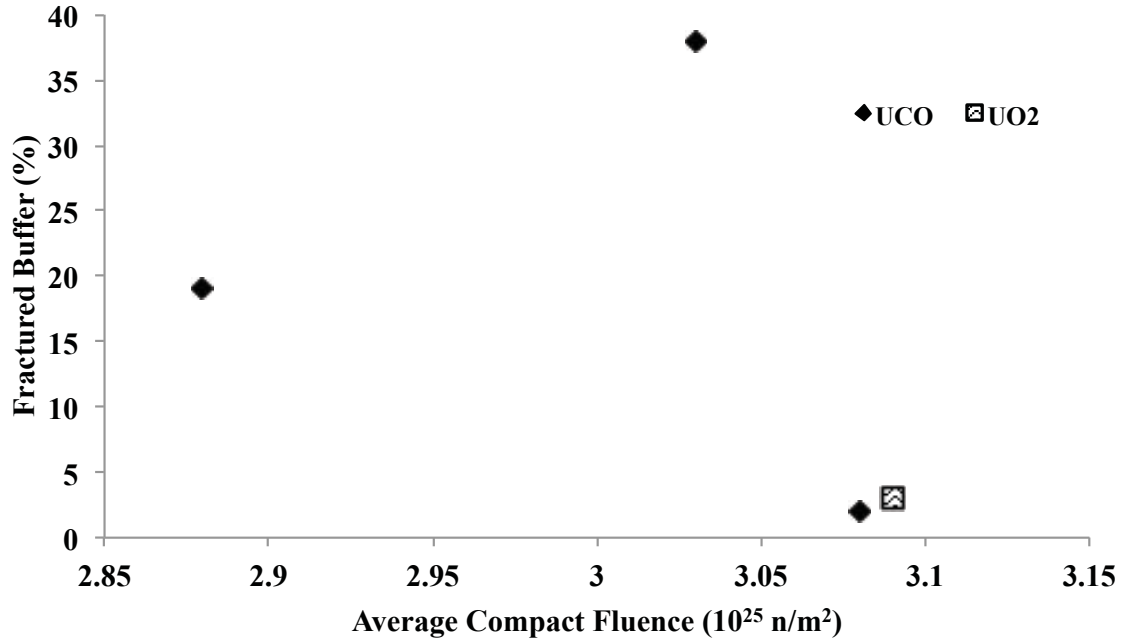


Figure 15. Buffer fracture frequencies relative to fast neutron fluence ($E > 0.18 \text{ MeV}$).

4.3.2 IPyC Tears

Analysis of the three dense outer coating layers (i.e., IPyC, SiC, and OPyC) is a key component of evaluating fuel performance, as these layers provide retention of fission products in the fuel. A few tangential IPyC tears were observed, with examples shown in Figure 16. The most severe tear that was observed in all the AGR-2 particles characterized is highlighted to the right in Figure 16. IPyC tears usually appear to have been caused by buffer-IPyC delamination (similar to what was observed previously for the AGR-1 particles), and are often observed in the absence of any visible buffer fractures as in (Figure 16). IPyC tears are fairly limited in their extent and were not observed to propagate all the way through the IPyC layer in any of the particles analyzed. In particles with partial buffer-IPyC delamination, stresses in the IPyC may be concentrated at a point where the buffer is still attached to the IPyC and can initiate tearing of the IPyC layer. The IPyC tear shown on the right in Figure 16 appears to be at the point where the buffer-IPyC interface transitions from bonded to unbonded. The tear shown on the left apparently originated in a similar manner, but the buffer-IPyC debonding subsequently continued past this location. A summary of IPyC tear frequency relative to the particle sub-type is given in Table 6 for each AGR-2 compact. IPyC tear frequencies for the aggregate of AGR-2 UCO compacts are summarized in Table 7.

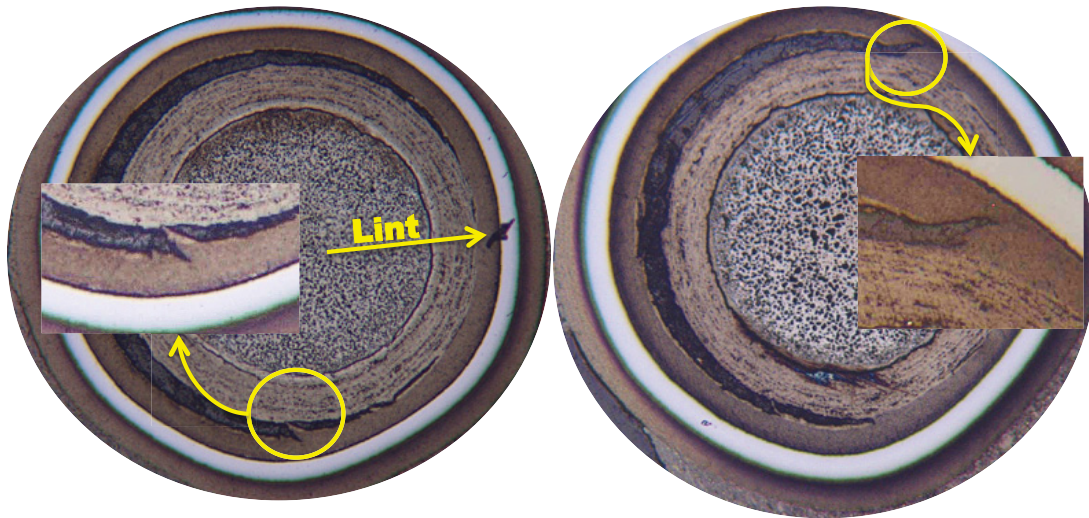


Figure 16. AGR-2 fuel particle IPyC tear examples. Particles shown are 213-68X-20 (left) and 213-69X-28 (right).

Table 6. Summary of the IPyC fracture data from sub-category type particles found in the AGR-2 compacts. The percentages of IPyC tears are relative to the number of particles in the sub-category type.

Particle Sub-Type	Compact / Fuel Type / TAVA							
	2-1-3 / UCO / 1194		2-4-3 / UCO / 1216		3-2-3 / UO ₂ / 1045		5-1-3 / UCO / 1078	
	Sub-Type Total	Tear Frequency %	Sub-Type Total	Tear Frequency %	Sub-Type Total	Tear Frequency %	Sub-Type Total	Tear Frequency %
Ai	94	2	94	0	56	2	61	0
Af	28	7	3	0	1	0	44	5
ABi	68	6	62	10	42	2	50	8
ABf	8	0	0	0	2	0	26	0

Table 7. Summary of the total AGR-2 UCO compact IPyC fracture data. The percentages of IPyC tears are relative to the number of particles in the sub-category type.

Sub-Particle type	Number of particles for each type	Number with partial IPyC tears	
		Particles with tears	Tear frequency %
Ai	249	1	0.4
Af	75	4	5.3
ABi	179	14	7.8
ABf	35	0	0.0

Figure 17 highlights a commonly-observed behavior with respect to buffer-IPyC delamination. Often the buffer-IPyC interface itself does not fail, but the buffer layer near the IPyC layer tears, leaving a small portion of the buffer attached to the IPyC layer. Like the UCO particle in Figure 17, Figure 18 also highlights the same behavior with respect to buffer-IPyC delamination in UO₂.

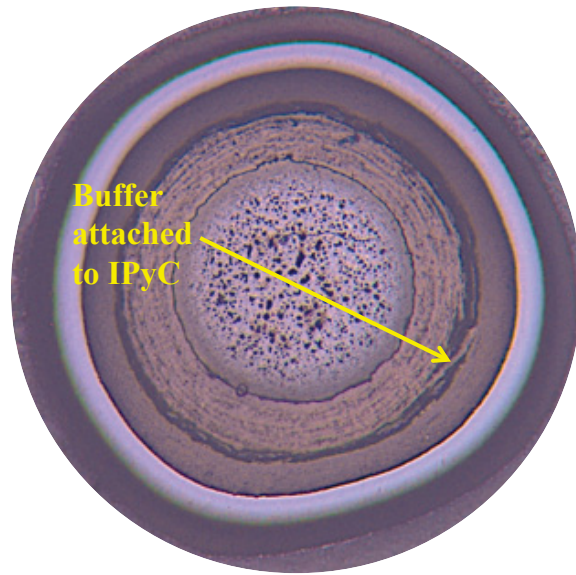


Figure 17. An example of an Ai particle (243-58X-57) with a buffer strip still attached to the IPyC at a tear location.

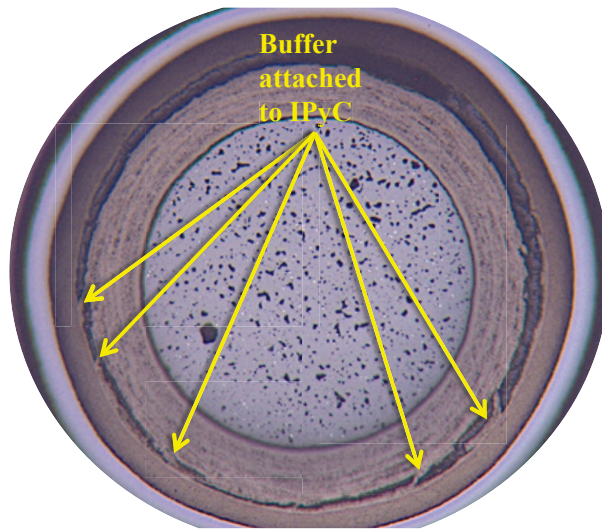


Figure 18. Particle 323-63X-3 with Type Ai characteristics showing the typical UO_2 fuel kernel morphology with the buffer intact with small strips of buffer adhered to the IPyC.

4.3.3 SiC and OPyC Observations

No SiC or OPyC fractures were observed in the AGR-2 UCO and UO_2 cross sections characterized. With the exception of the single UO_2 particle shown earlier in Figure 10 (where the IPyC layer debonded from the SiC layer), no unusual features were detected for either the SiC or OPyC layers for the compacts characterized.

4.4 Fuel Kernel Observations and Behaviors

4.4.1 Qualitative Observations

It was noted previously in AGR-1 particles that a carbide skin was formed on the fuel kernels during fabrication, and that evidence of the remnants of this thin layer could often be observed on the irradiated particles (Reference 8). Figure 19 of particle 213-68X-1 is a good example of this in the AGR-2 UCO fuel. Additionally, note the circumferential cracks that form perhaps due to the different material properties at this buffer-to-kernel interface. Figure 20 shows a light, halo-like appearance around the inside of the buffer at the UO_2 kernel-buffer interface; however, there is no evidence that carbide skins form on UO_2 kernels. This halo does appear to have less porosity than the rest of the buffer. Halos similar to this were observed in AGR-2 UO_2 particles and can be observed in UO_2 particle micrographs throughout this report. The dark line around the UO_2 fuel kernel appears to be a shadow or narrow gap between the kernel and the buffer likely caused by rounding during specimen polishing of the soft pyrocarbon layer in contrast to the harder kernel.

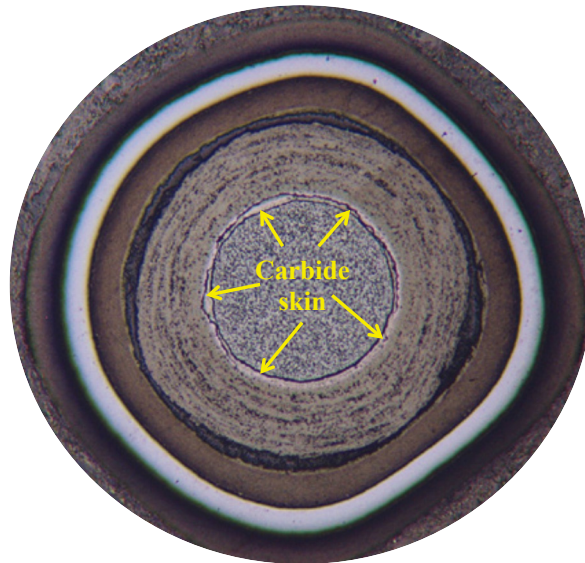


Figure 19. UCO Particle 213-68X-1 showing the carbide skin.

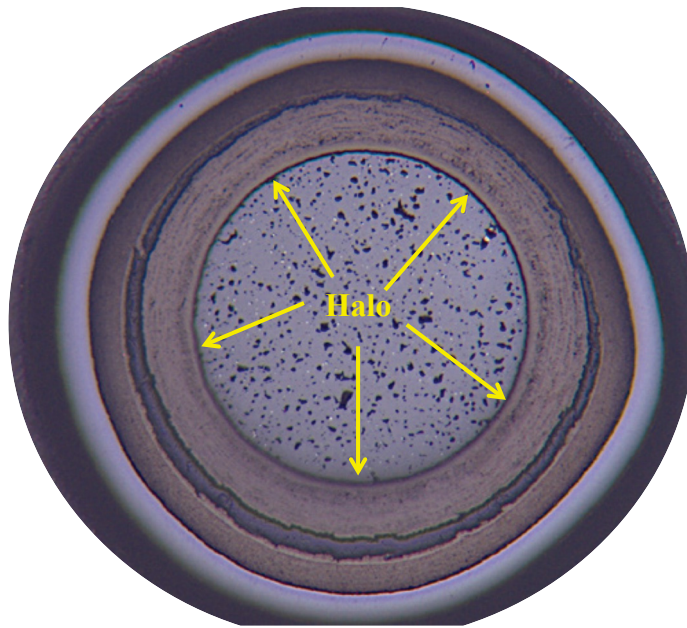


Figure 20. UO₂ Particle 323-61X-13 showing a thin halo at the kernel-buffer that appears to have reduced porosity.

Figure 21 shows crack propagation through porosity in a fuel kernel from UCO Compact 2-1-3. Cracks similar to this example were evident in some particles in all the UCO compacts. Similar features, shown in Figure 22, were found in UO₂ fuel kernels from Compact 3-2-3. It is not known whether the kernel cracks are due to irradiation or are an artifact of sample preparation.

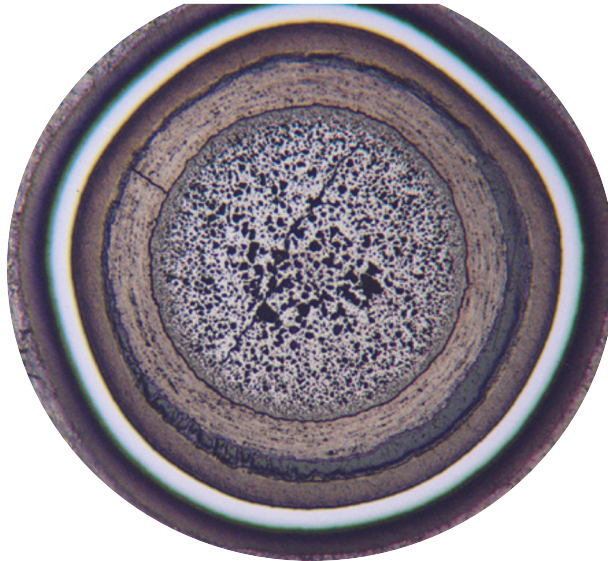


Figure 21. UCO particle 213-69X-6 showing fuel kernel crack.

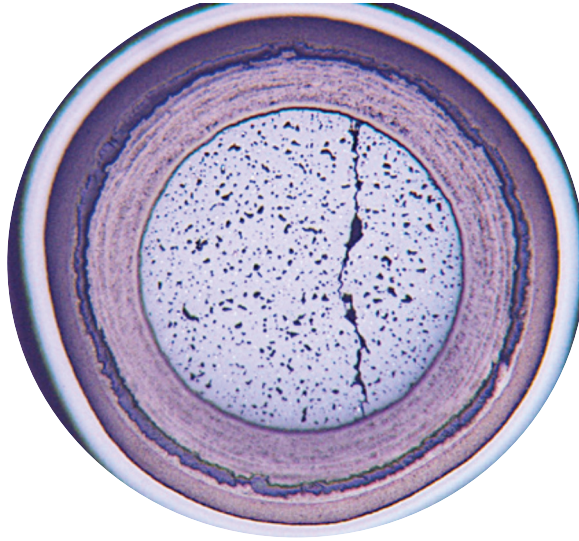


Figure 22. Particle 323-63X-7 with a fuel kernel crack.

4.4.2 Fuel Kernel Swelling

Fuel kernel swelling (also called kernel expansion) may be somewhat constrained if the buffer layer remains intact, as in Figure 23. However, in the case of UCO particle buffer layer fractures, the kernel can expand into the radial gap in the fractured buffer, as in Figure 24. Note that in Figure 24, there is a wide variation in the degree of kernel expansion in the radial gap left behind by buffer fracture. It is hypothesized that the extent of fuel kernel expansion into a buffer crack observed at the end of irradiation is related in part to the timing of the fracture during irradiation, where an earlier crack occurrence would allow more time for fuel to expand into a fracture region. Fuel kernel expansion also impacts the kernel porosity, discussed in Section 4.4.3

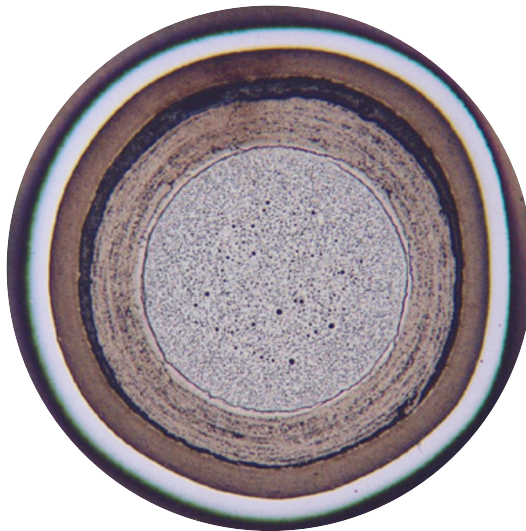


Figure 23. Particle 513-65X-53 with Type Ai characteristics showing the typical UCO fuel-kernel morphology, intact buffer, and complete buffer-IPyC debonding.

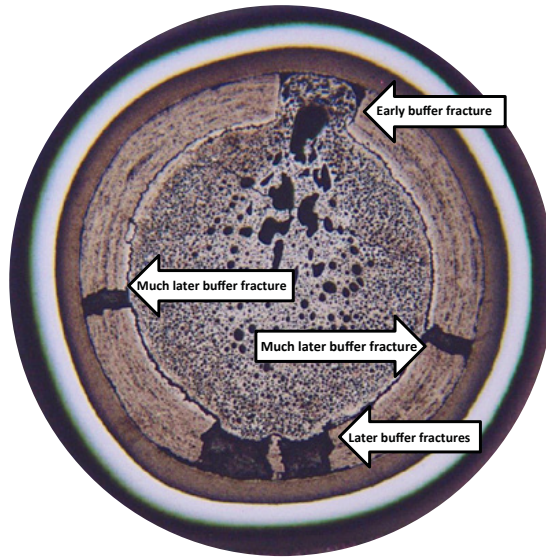


Figure 24. Particle 513-65X-4 with Type Af characteristics showing the typical UCO fuel-kernel morphology with the buffer fractured in several locations.

Only four UO_2 particles with fractured buffers were found, and in each case (in contrast to the behavior observed in UCO particles), the buffer fractures were so narrow that kernel expansion into the cracks was not observed. Figure 12 above was one such example of buffer fracture in UO_2 particles. Figure 25 shows two other UO_2 particles with fractured buffers. In both particles in Figure 25, the buffer cracks are narrow, the kernel did not expand into the cracks, and the fuel appears to be as well-constrained here, as in the other UO_2 particles with no buffer fractures. The radial buffer cracks in the particle shown in Figure 25 may have occurred during sample preparation; however, it is believed that these cracks occurred during irradiation because cracking from sample preparation would be expected to be more widespread throughout the mounts.

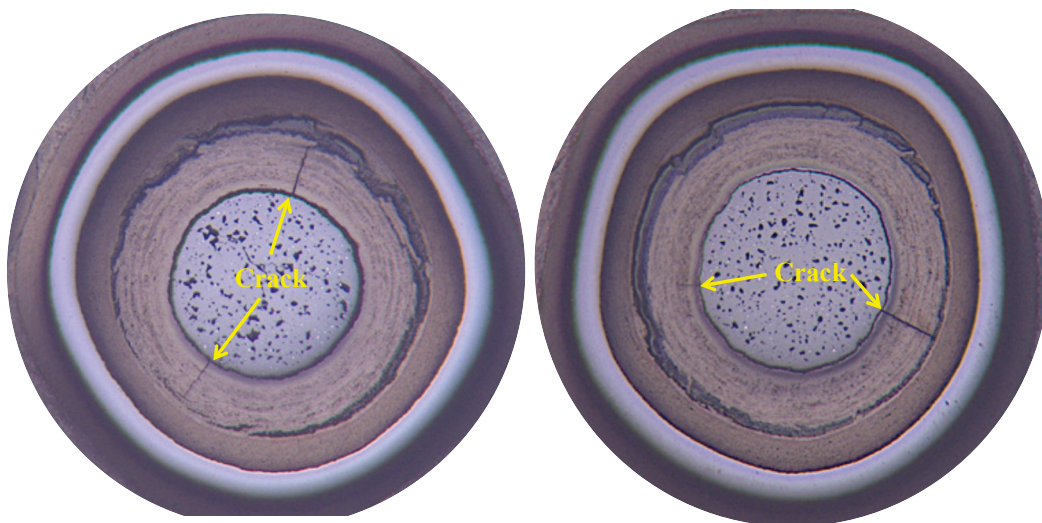


Figure 25. At left, Particle 323-63X-5 (Type ABf) showing the typical UO_2 fuel kernel morphology with two narrow, radial buffer cracks. At right, Particle 323-62X-27 (Type Af) with a single through-layer radial buffer crack and a partial crack.

4.4.3 Fuel Kernel Pore Sizes

In the UCO fuel kernels, pore size relative to location within the kernel was largely influenced by buffer constraint on kernel swelling. As shown previously in Figure 24, where the fuel kernel was locally unconstrained due to buffer fracture, pore size grew in the kernel center and in regions where fuel had fully expanded into a large crack. For comparison, Figure 26 illustrates a UCO particle without buffer fracture, showing centrally located pores that are smaller than those found in particle 513-65X-4 (Figure 24). The different pore structures in particles with fractured buffers and those with intact buffers, is a consistent feature among UCO particles.

Irradiation temperature may also have an effect on kernel porosity. In UCO particles with buffer fractures, the apparent kernel porosity observed in compacts from the hottest capsule (Capsule 2) was comparable to that observed in the cooler capsule (Capsule 5). However, in the absence of buffer fractures, the porosity in Capsule 2 kernels (for example in Figure 26) was generally greater than that in Capsule 5 kernels (for example in Figure 23). This could be attributed to the higher irradiation temperature in Capsule 2. Furthermore, the number and size of the pores is generally larger in the center of UCO kernels than in UO_2 kernels (especially in kernels from the hotter Capsule 2 compacts). Factors that could influence this behavior are the higher burnup and generally higher irradiation temperature of the UCO fuel compared to the UO_2 fuel and the differences in chemical/thermophysical properties between a UCO kernel and a UO_2 kernel. As evidenced in Figure 27, the UO_2 fuel's pore spatial distribution appears to be more random, and the pore sizes generally smaller compared to UCO kernels. In a minority of UO_2 particles, (such as the UO_2 particle in Figure 22) a crack in the kernel may have developed and propagated through kernel porosity. Substantially fewer kernel cracks were observed in UCO kernels than in the UO_2 kernels. It is not known if these cracks are due to irradiation or an artifact of sample preparation.

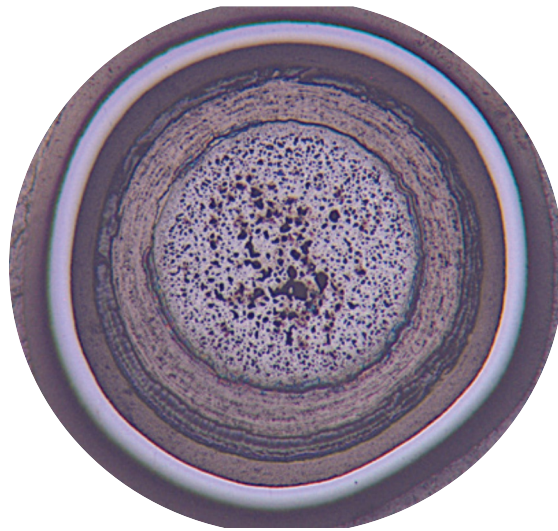


Figure 26. Particle 243-60X-16 with Type Ai characteristics showing the typical UCO fuel-kernel pore morphology when the buffer remained intact.

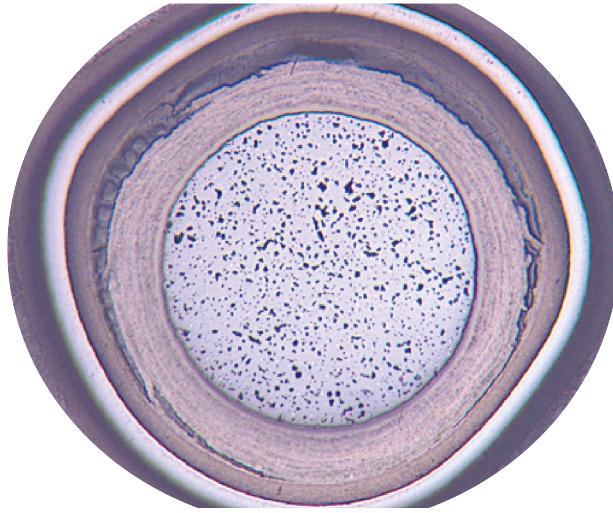


Figure 27. Particle 323-61X-32 with Type ABi characteristics showing a typical UO_2 fuel-kernel porosity distribution.

4.5 Particle Type Spatial Distribution

Particle maps, shown in Figure 28 through Figure 31 for each fuel compact cross section, were created with shades of gray assigned per particle type according to Figure 5. Maps for some UCO compact cross sections reveal a non-uniform spatial distribution of particle types. Note that particles with fractured buffers are assigned a darker shading. The straight portion of the dashed half-circles crossing the mid-point of the disc outlined on the center radial cross sections indicates the axial plane examined for the top and bottom cross sections. In Figure 28, Compact 2-1-3 exhibits a slightly increased concentration of fractured buffers in the left sides of the longitudinal cross sections. A higher concentration of buffer fractures is seen in the lower portion of the radial cross section (MNT 67X in Figure 28) toward the left and right edges (especially the left edge) of the longitudinal cross-section MNT 69X, and toward the left and top edges of longitudinal cross-section MNT 68X. Due to the very low fraction of buffer fractures, a trend in particle morphology is not immediately apparent in the cross sections from Compact 2-4-3 in Figure 29. The two particles with fractured buffers observed in Figure 29 were located near the outer edges of the compact. Compact 5-1-3 exhibits a pronounced concentration of fractured buffers in the lower longitudinal cross section (MNT 65X in Figure 30) and on the right side of the radial cross section (MNT 64X).

Given the overall trend of increasing buffer fracture frequency with increasing irradiation temperature (Figure 14), it is possible that the non-uniform distribution of buffer fractures in the 2-1-3 and 5-1-3 cross sections are due to thermal gradients within the compacts during irradiation. Based on the time-average temperatures of these compacts (minimum, volume-average, and maximum) shown in

Table 1, it is clear that temperatures could vary considerably within a compact throughout the course of irradiation. Detailed modeling of the temperatures within the compacts using finite element analysis¹¹ indicates that radial temperature gradients across a single compact can exceed 100°C , and axial gradients may approach 300°C . Compacts have higher temperatures on one side (i.e., the side oriented toward the center of the capsule), as well as gradients along the axial length (with temperatures tending to be higher in the center of a compact stack and decreasing toward the top and bottom of a stack). These trends seem consistent with the observed distribution of buffer fractures in Compact 5-1-3 (Figure 30), where there is a much higher frequency at the bottom of the compact and to one side. As Compact 5-1-3 was located at

the bottom of Capsule 5 during irradiation, it is expected that the bottom of this compact was at a lower temperature than the top, with a correspondingly higher fraction of buffer fractures. While the azimuthal orientation of the compact relative to its orientation in the irradiation capsule is not known, a higher fraction of buffer fractures to one side is consistent with a lower temperature on the side of the compact facing away from the center of the irradiation capsule and a higher temperature on the side of the compact facing the center of the capsule. The implication is that the side of the Compact 5-1-3 radial cross section with fewer buffer fractures (i.e., the left side of MNT 64X in Figure 30) is the side that was facing the center of the irradiation capsule during irradiation, and therefore experienced higher temperatures, which enabled creep relaxation of stresses in the buffer layers.

While the non-uniformity in spatial distribution of buffer fractures in Compact 2-1-3 (Figure 28) is less pronounced than Compact 5-1-3 (Figure 30), it appears to follow a similar trend that is consistent with expected thermal gradients. Specifically, buffer fractures in Compact 2-1-3 are concentrated on the bottom side of the radial cross section and also to one side of the longitudinal cross sections, and this side of the compact presumably was oriented away from the center of the capsule and experienced lower temperatures. There was a very low fraction of buffer fractures in the UO_2 particles, and no clear trend is apparent in the Compact 3-2-3 cross sections (Figure 31), although the few fractures that were observed appeared on the left and right edges of the longitudinal cross sections.

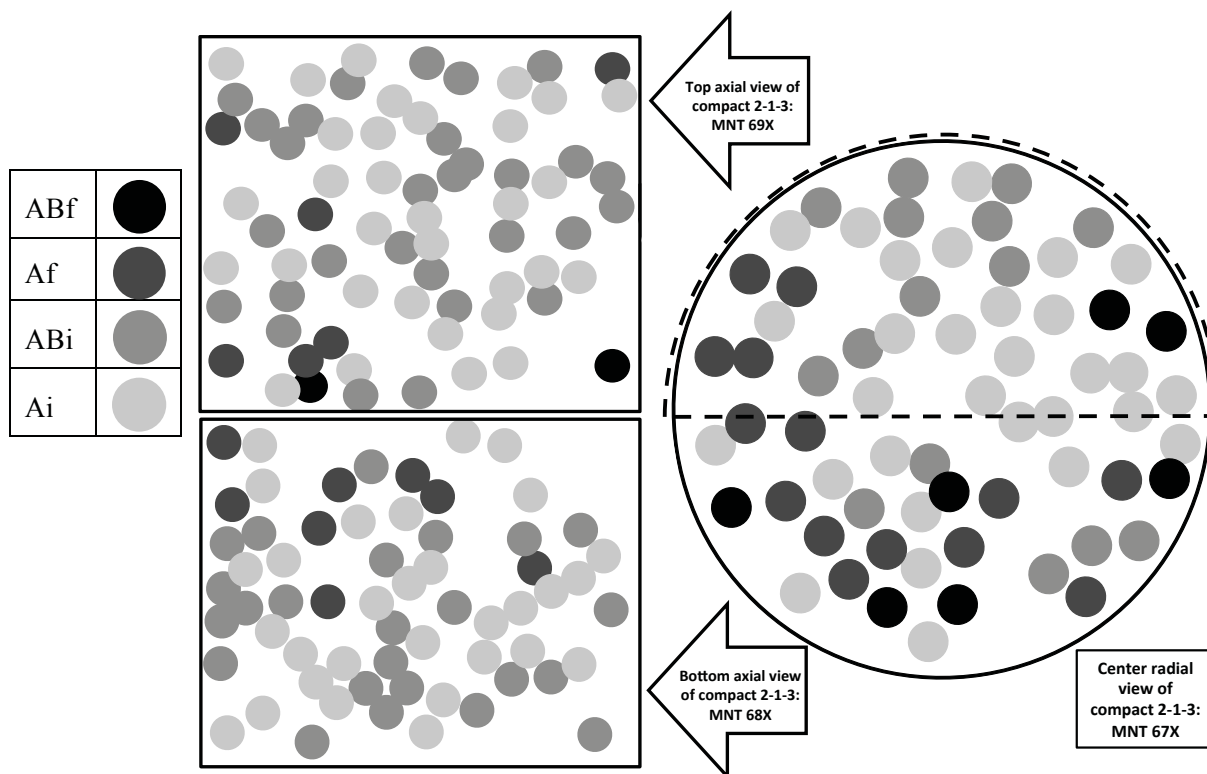


Figure 28. Compact 2-1-3 grayscale particle types showing evidence of a buffer failure gradient likely due to a temperature gradient within the compact. Relative to the cutting diagram (Figure 2), MNT 69X is piece #2, MNT 67X is piece #1 and MNT 68X is piece #3.

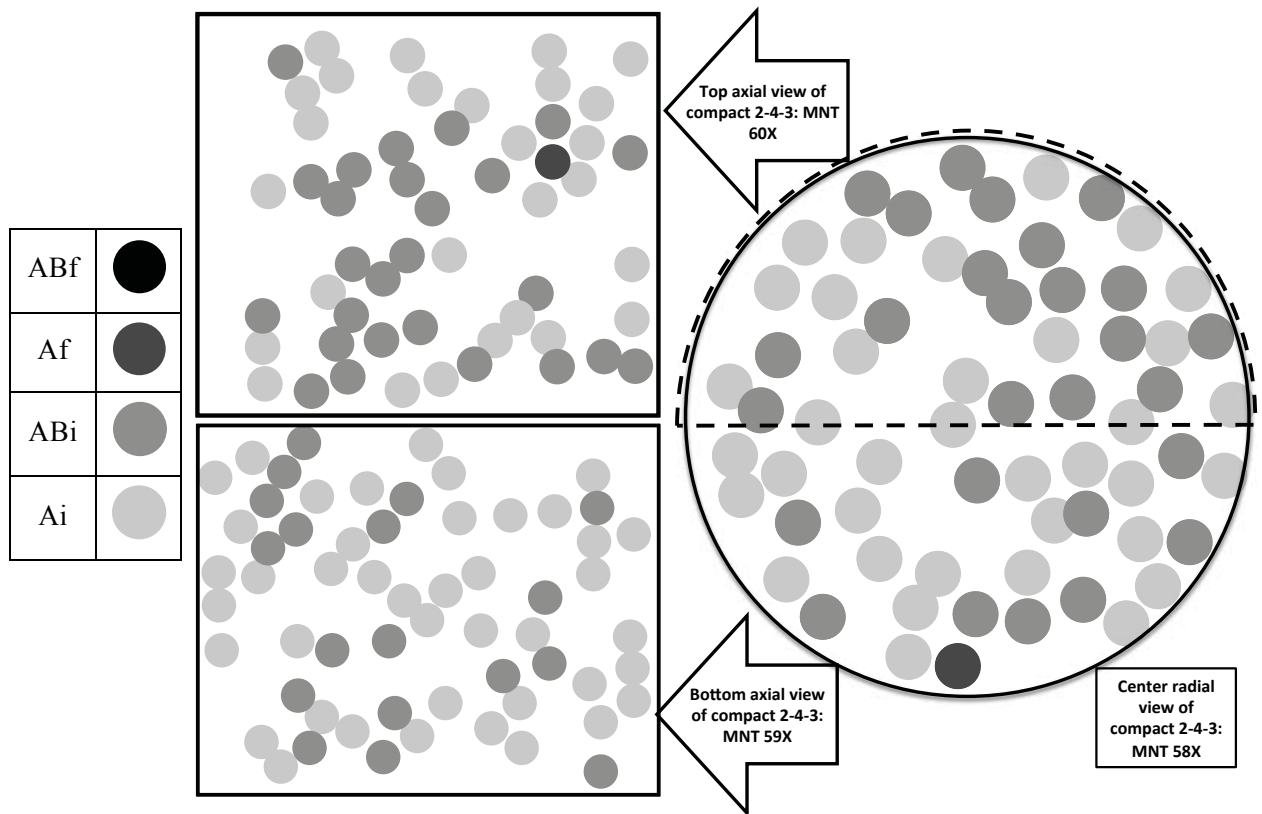


Figure 29. Compact 2-4-3 grayscale particle types. Relative to the cutting diagram (Figure 2), MNT 60X is piece #2, MNT 58X is piece #1 and MNT 59X is piece #3.

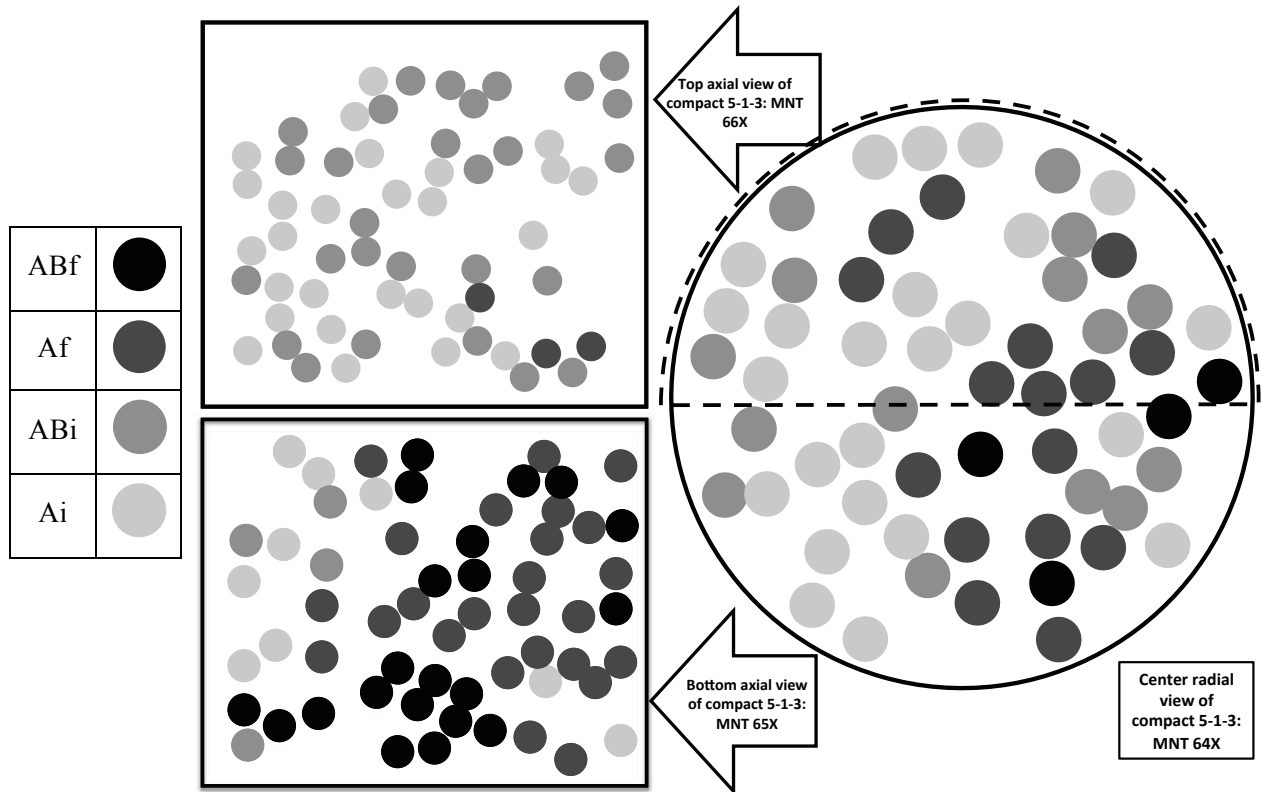


Figure 30. Compact 5-1-3 grayscale particle types showing evidence of a buffer failure gradient likely due to a temperature gradient within the compact. Relative to the cutting diagram (Figure 2), MNT 66X is piece #2, MNT 64X is piece #1 and MNT 65X is piece #3.

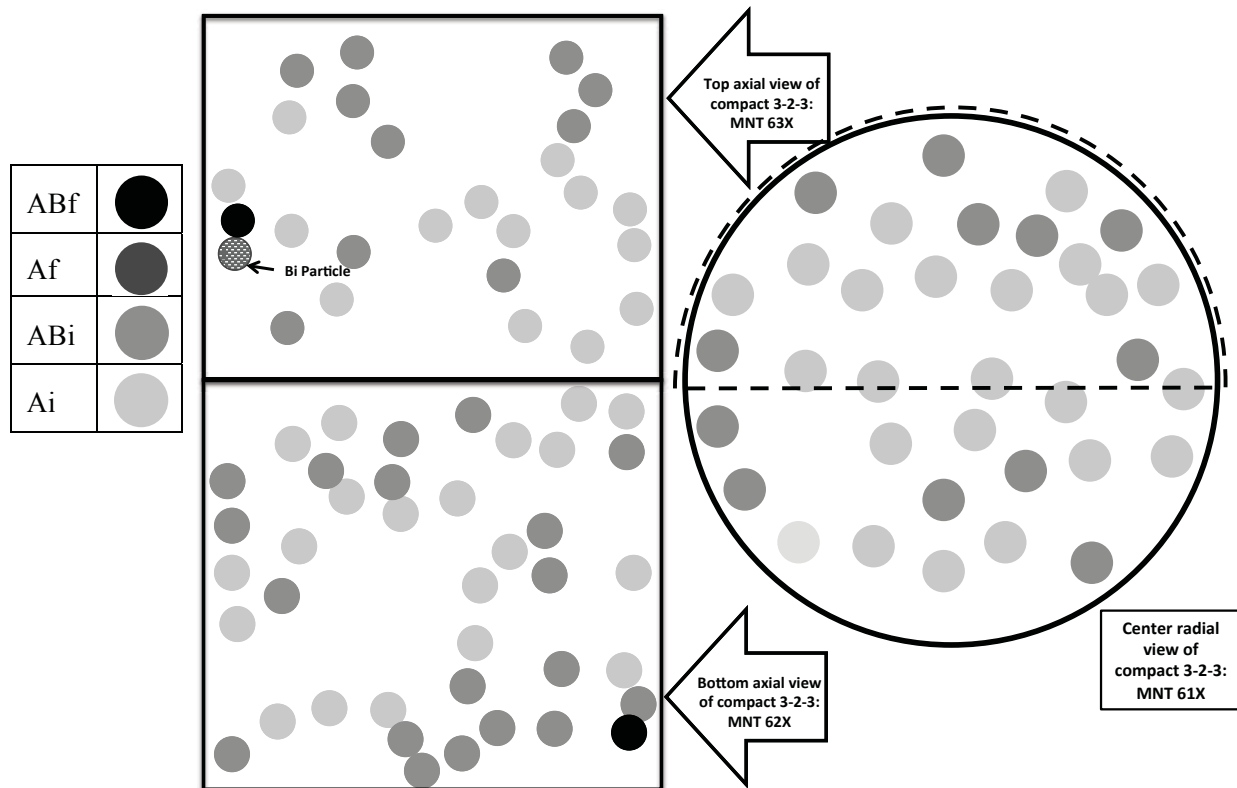


Figure 31. Compact 3-2-3 grayscale particle types. Relative to the cutting diagram (Figure 2), MNT 63X is piece #2, MNT 61X is piece #1 and MNT 62X is piece #3.

5. AGR-2 and AGR-1 UCO PARTICLE COMPARISONS

Differences in the UCO fuel particle coating behaviors between AGR-1 and AGR-2 were observed. Specifically, differences were seen between the number of buffer fractures and how the buffer layer behaviors influenced the IPyC layer. Six AGR-1 compacts were characterized³. Fuel-kernel swelling and porosity morphologies did not differ noticeably between AGR-1 and AGR-2.

5.1 Particle Types

A total of 538 UCO particles were characterized for AGR-2, as compared to 981 for AGR-1, with an average of 179 and 163 particles characterized per compact, respectively. (The difference in number of average particles per compact may be due largely to the lack of fuel-free end caps in the AGR-2 fuel compacts, giving slightly more volume occupied with particles compared to AGR-1.) Particle types for the AGR-1 UCO fuel compacts and AGR-2 compacts are summarized Table 8. The absence of AGR-2 Type B particles is apparent in Table 8. This result suggests that the longer fluidization time prior to the AGR-2 buffer coating application was effective in weakening the buffer-IPyC bond, allowing the buffer to separate more easily from the IPyC layer. Figure 32 illustrates a reduction in AGR-2 Ai, B and ABf type particles and an increase in Af and ABi type particles compared to AGR-1.

Table 8. AGR-2 and AGR-1 UCO particle type summary.

EXPERIMENT	Type A		Type B		Type AB		Compact Total Particles
	Ai / percent	Af / percent	Bi / percent	Bf / percent	ABi / percent	ABf / percent	
AGR-2 Totals (3 UCO compacts examined)	249 / 46	75 / 14	0 / 0	0 / 0	179 / 33	35 / 7	538
	324 / 60		0 / 0		214 / 40		
AGR-1 Totals (6 compacts examined)	520 / 53	79 / 8	45 / 5	8 / 1	187 / 19	142 / 14	981
	599 / 61.1		53 / 5.4		329 / 33.5		

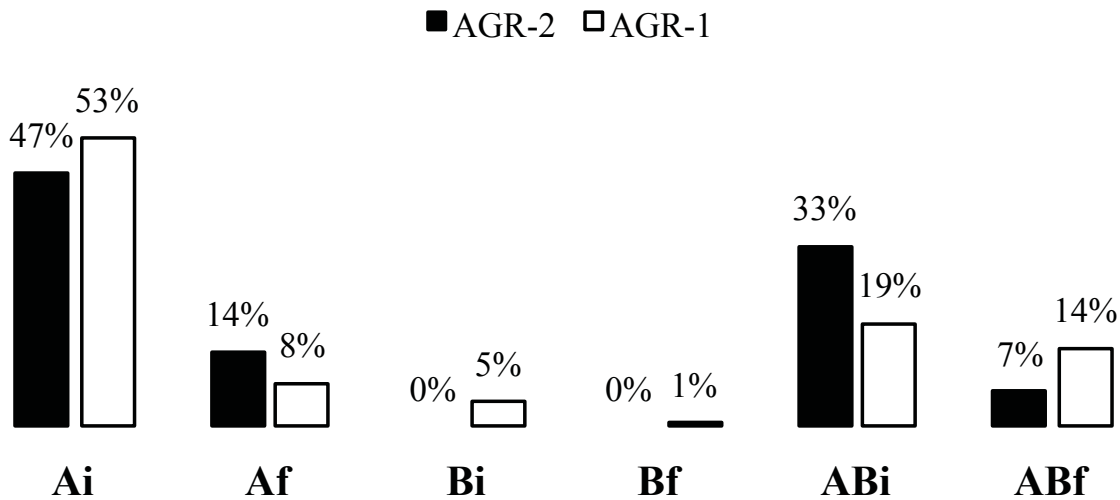


Figure 32. Comparison of UCO particle sub-types between AGR-2 and AGR-1.

5.2 Buffer Fractures

Figure 33 shows the contrast between buffer-fracture frequency for AGR-1 and AGR-2, combining the A and AB particle types. While there were relatively minor differences in the number of particles with buffer fractures (with slightly more in AGR-1), the overall fractions appear fairly similar. Figure 34 illustrates buffer fractures relative to compact irradiation temperature. While the three data points from AGR-2 indicate an inverse relationship between temperature and buffer fracture occurrence, the AGR-1 data fail to demonstrate a trend over their respective range of irradiation temperatures. If the decreased buffer fracture frequency in the higher-temperature AGR-2 compacts is indeed the result of higher temperatures, allowing better relaxation of stresses in the layer through thermal creep, the data in Figure 34 may indicate a threshold temperature for this effect of approximately 1100-1150°C, with AGR-1 compacts all falling below this temperature threshold.

However, potential differences in the buffer properties between AGR-1 and AGR-2 may play a role in the observed behavior (i.e., buffer density, which was not accurately measured for AGR-2 but appears to be slightly lower than AGR-1 [Ref. 2]). Furthermore, particle geometry differences between AGR-1

and AGR-2 UCO fuel (i.e., 350 vs. 425 μm nominal kernel diameters, resulting in a volume increase of approximately 79% for the AGR-2 kernels and a reduction in the layer curvature) may also play a role.

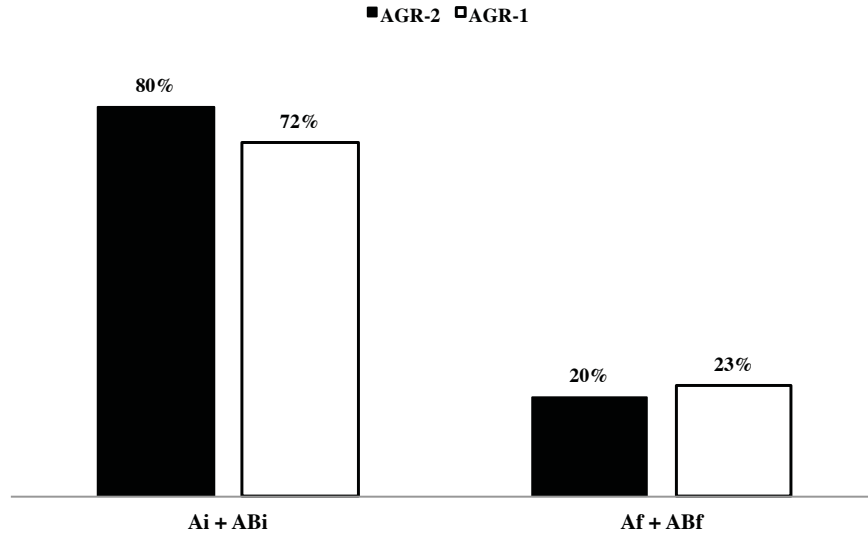


Figure 33. Buffer fracture frequency relative to particle attribute type. Recall that 5% of AGR-1 particles were type Bi particles.

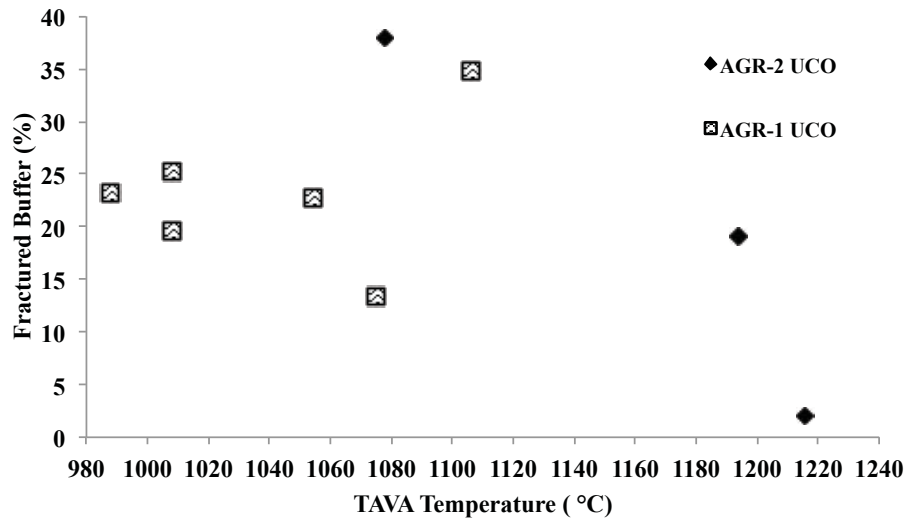


Figure 34. Percentage of particles with fractured buffers for AGR-2 and AGR-1 UCO compacts.

Besides the somewhat lower frequency of buffer fractures in AGR-2 compared to AGR-1, the non-uniformity of the spatial distribution of buffer fractures in the AGR-2 compact cross sections (discussed in Section 4.5) differs from the observations of AGR-1, in which no such gradients were observed. This, again, may indicate that there is a threshold temperature, above which buffer fracture is less likely, and that AGR-1 fuel was irradiated at temperatures that were predominantly below this threshold.

In particles with fractured buffer layers, the distribution of cracks within the buffer differed between AGR-1 and AGR-2. Figure 35 shows (at left) a typical buffer fracture pattern for AGR-1 particles and (at right) a common AGR-2 buffer fracture pattern. For AGR-1 particles with fractured buffers, nearly all of them showed two diametrically-opposed buffer cracks. In contrast, very few AGR-2 particles with

fractured buffers showed this pattern. The overwhelming majority of buffer-fractured AGR-2 particles had four or five cracks in the buffer, such as were observed in the particle at right in Figure 35. Very few AGR-2 particles exhibited the AGR-1 buffer fracture pattern of two diametrically-opposed cracks. The fact that AGR-2 buffer layers tended to fracture with more cracks than AGR-1 buffers suggests that AGR-2 buffers fracture at lower creep-strains than in AGR-1.

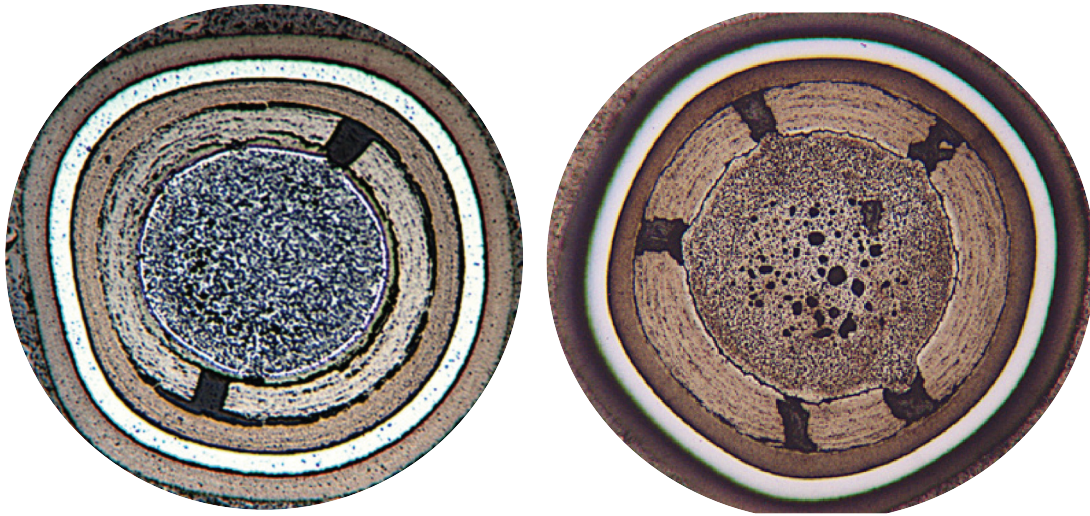


Figure 35. AGR-1 particle 213-138T-55 (left) and AGR-2 particle 513-65X-9 (right).

5.3 IPyC Tears

A significant difference in irradiated particle appearance between AGR-1 and AGR-2 was the absence of through-fractures in the AGR-2 IPyC layers in the particles observed. Only a few tangential IPyC tears were observed in AGR-2 with the most severe example shown on the right in Figure 36 (also shown earlier at right in Figure 16). This is compared to IPyC fractures and tears observed in a selected AGR-1 particle from Reference 3, as shown on the left in Figure 36a. Many AGR-1 particles with IPyC tears were correlated with buffer-fracture locations. These propagated perpendicular to the buffer-to-IPyC bond region out from buffer fractures in regions apparently well-bonded to the IPyC. These types of IPyC fractures were absent in the cross sections examined for AGR-2. Like many AGR-1 tangential tears associated with a strong buffer-to-IPyC bond, AGR-2 IPyC tears also appear to be attributed to the strength of this interface.

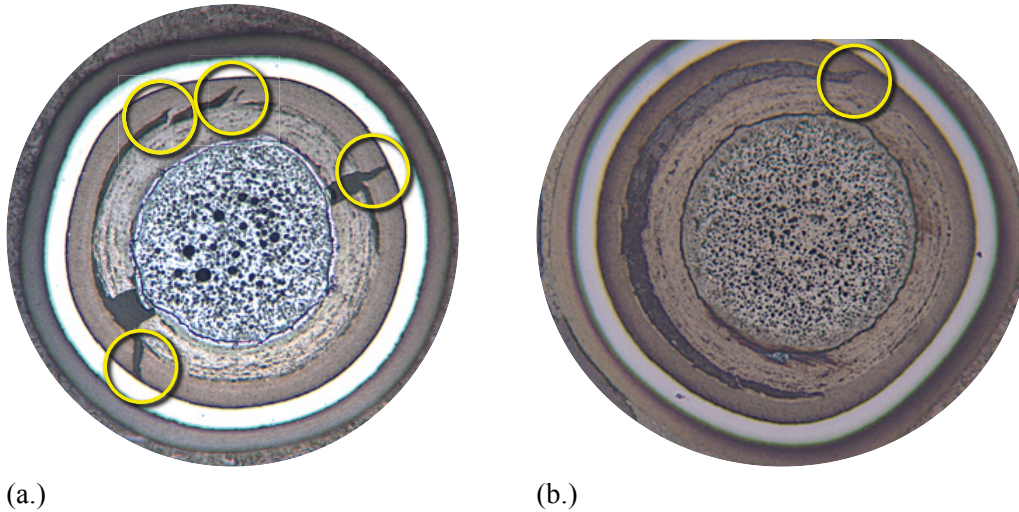


Figure 36. (a.) AGR-1 Particle 333-56T-50 showing multiple IPyC fractures with two associated with buffer fractures. (b.) AGR-2 Particle 213-69X-28 showing the most severe IPyC tear observed in the AGR-2 compact cross sections.

A comparison of IPyC tear frequencies relative to the particle sub-types is shown in Figure 37 for the AGR-2 and AGR-1 compacts. This figure shows the partial and through-tears for AGR-1 as compared to the few partial and zero through-tears for AGR-2. Note that 100% of the tears in the Type B particles for AGR-1 traversed the entire IPyC layer. The lower incidence of IPyC fractures, the higher total fraction of Type A and Type AB particles, and the almost complete absence of Type B particles in the AGR-2 cross sections, suggests that separation of the buffer and IPyC layers occurred more readily in the AGR-2 particles than in AGR-1 particles. It is currently believed that this may be the result of the longer fluidization time between buffer and IPyC layer deposition that was used in the AGR-2 particle fabrication process compared to the AGR-1 fabrication parameters. Given the dominant SiC failure mechanism that was identified for the AGR-1 fuel (precipitated by IPyC fracture as a result of buffer densification and a sufficiently strong buffer-IPyC bond, as discussed in Reference 6), it is suspected that SiC failures by this mechanism in the AGR-2 particles will have a lower incidence compared to AGR-1. Destructive examination and safety testing of the fuel compacts will help to elucidate this aspect of the AGR-2 fuel performance to a greater degree.^{3,12}

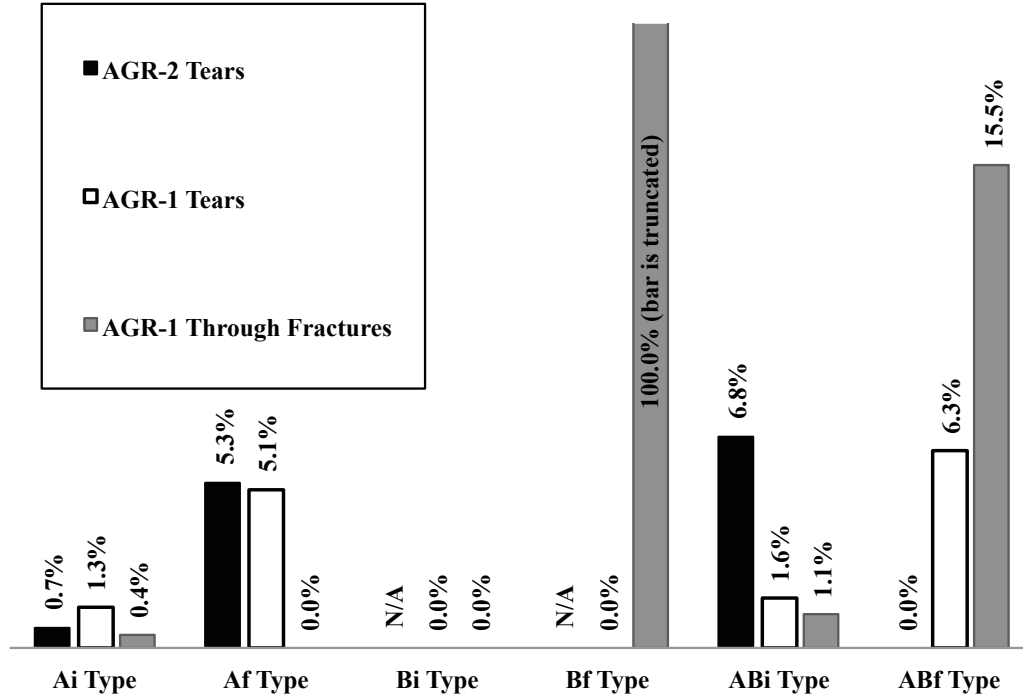


Figure 37. Comparison of the percentages of each particle type that exhibited IPyC tears for AGR-1 (through and partial tears are shown separately) and AGR-2.

6. Conclusions

The examined AGR-2 UCO compact cross-sectional surfaces demonstrate that the characterized particles performed in a manner generally consistent with UCO fuel previously analyzed from AGR-1. Several differences between AGR-1 UCO fuel behavior and AGR-2 UCO fuel behavior were noted.

1. In particles with fractured buffer layers, AGR-2 buffer layers typically had 4 or 5 radial buffer cracks; however, AGR-1 buffers typically had two diametrically opposed radial buffer fractures. This could indicate that AGR-2 buffers fracture at lower creep-strains than in AGR-1.
2. Non-uniform spatial distributions of buffer fractures within some AGR-2 UCO compact cross sections were observed in contrast to no apparent spatial variation within the AGR-1 compact cross sections.
3. The frequency of AGR-2 buffer cracking was observed to decrease with increasing TAVA irradiation temperature (from 38% fracture at 1080°C to 2% fracture at 1220°C).

The data suggest that higher irradiation temperatures may reduce buffer-fracture occurrences in the UCO fuel, possibly due to higher temperatures allowing thermal creep to relax stresses in the layer. These thermal effects on buffer fracture may have a threshold temperature (near 1100°C) below which thermal creep is unable to adequately relieve stress in the layer and prevent fracture (as in the lower irradiation temperatures of AGR-1). Additionally, the thermal gradients within the compacts during the AGR-2 irradiation likely drove the observed spatial variation of buffer cracking within the compacts. The AGR-2 fabrication parameters, including a longer fluidization time between buffer deposition and

deposition of the IPyC layer, appear to have promoted beneficial buffer-IPyC separation to a greater extent than observed in AGR-1 particles. One result is the complete absence of full IPyC layer fractures in the AGR-2 particles examined in this study, and a reduced severity of tears in the IPyC relative to AGR-1 particles. Given the good overall performance of the AGR-1 fuel during irradiation and post-irradiation safety testing⁶, the reduced occurrence of full IPyC fractures in AGR-2 compared to AGR-1 suggests that good fuel performance (particularly in terms of low fission product release and low total SiC failure fractions) should be expected with AGR-2.

No typical Type B particle characteristics were noted in AGR-2 in either UO₂ or UCO fuel such as those that were observed in AGR-1 UCO fuel. The only Type B particle found was a UO₂ particle that was atypical due to a complete debond of the IPyC from the SiC layer (the first such particle observed in either AGR-1 or AGR-2). All layers in this particle were found to be intact in the plane observed.

While the buffer fracture frequency in the AGR-2 UCO fuel was found to decrease with increasing irradiation temperature, the limited range of irradiation conditions for fuel compacts in the single AGR-2 UO₂ capsule make determining correlations with temperature, burnup, and fluence challenging for the UO₂ fuel. However, data from the single UO₂ fuel compact presented here suggests that buffer fracture was less likely in the UO₂ fuel than the UCO fuel. UO₂ particles with buffer cracks had very narrow buffer cracks which did not demonstrate kernel expansion into the cracks. In contrast, buffer cracks in UCO particles generally were sufficiently wide that kernel expansion into the cracks was often observed. UO₂ kernel porosity was generally smaller and more uniformly distributed throughout the kernel, but UCO kernel porosity was generally larger and localized more in the center of the kernel. The factors contributing to these observed differences are not known at this time, but may include differences in radiation-induced kernel swelling rates between UO₂ and UCO and the lower burnup of the UO₂ fuel. For AGR-2 particles with intact buffer layers, the number and size of pores in UCO kernels were generally greater in particles from compacts with higher irradiation temperatures.

7. REFERENCES

- 1 D.A. PETTI, J.T. MAKI, J.D. HUNN, P.J. PAPPANO, C.M. BARNES, J.J. SAURWEIN, S.G. NAGLEY, J.M. KENDALL, and R.R. HOBBS, "The DOE Advanced Gas Reactor Fuel Development and Qualification Program," *JOM*, **62**, 62–66 (2010).
- 2 B.P. COLLIN, "AGR-2 Irradiation Experiment Test Plan," PLN-3798 Revision 1, Idaho National Laboratory (2011)
- 3 S.A. PLOGER, P.A. DEMKOWICZ, J.D. HUNN, J.S. KEHN, "Microscopic analysis of irradiated AGR-1 coated particle fuel compacts," *Nuclear Engineering and Design* **271**, 221-230 (2014)
- 4 J.D. HUNN, G.E. ELLISON Jr., and R.A. LOWDEN, "Increase in pyrolytic carbon optical anisotropy and density during processing of coated particle fuel due to heat treatment," *Journal of Nuclear Materials* **374**, 445-452 (2007).
- 5 B.P. COLLIN, "AGR-2 Irradiation Test Final As-Run Report," INL/EXT-14-32277, Revision 0, Idaho National Laboratory, 2014
- 6 P.A. DEMKOWICZ, J.D. HUNN, R.N. MORRIS, , I.J. VAN ROOYEN, T. GERCSAK, J.M. HARP, S.A. PLOGER, "AGR-1 Post Irradiation Examination Final Report," INL/EXT-15-36407
- 7 J.D. HUNN, "AGR-2 Fuel Compacts Information Summary: Prepared for the NRC MELCOR Project," ORNL/TM-2010/296, Revision 1, (2010)

-
- 8 P.A. DEMKOWICZ, J.D. HUNN, S.A. PLOGER, R.N. MORRIS, C.A. BALDWIN, J.M. HARP, P.L. WINSTON, T.J. GERCZAK, I.J. VAN ROOYEN, F.C. MONTGOMERY, C.M. SILVA, "Irradiation performance of AGR-1 high temperature reactor fuel," *Nuclear Engineering and Design*, **306**, 2-13 (2016).
 - 9 P.A. DEMKOWICZ, S.A. PLOGER, P.L. WINSTON, J.M. HARP, "AGR-1 Compact 1-3-1 Post-Irradiation Examination Results," INL/EXT-15-36365 DRAFT, Idaho National Laboratory (2016).
 - 10 J.D. HUNN, C.A. BALDWIN, F.C. MONTGOMERY, T.J. GERCZAK R.N. MORRIS, G.W.HELREICH, P.A. DEMKOWICZ, J.M. HARP J.D. STEMPIEN. "Initial Examinations of Fuel Compacts and TRISO Particles From The AGR-2 Irradiation Test", *Proc. 8th International Topical Meeting on High Temperature Reactor Technology*, Las Vegas, Nevada, USA, November 6-10 (2016)
 - 11 G.L. HAWKES, "AGR-2 Daily As-Run Thermal Analyses," ECAR-2476 Revision 1, Idaho National Laboratory, 2014
 - 12 R.N. MORRIS, J.D. HUNN, C.A. BALDWIN, P.A. DEMKOWICZ, "Initial results from safety testing on US AGR-2 irradiation test fuel," *Proc. 8th International Topical Meeting on High Temperature Reactor Technology*, Las Vegas, Nevada, USA, November 6-10 (2016)

Appendix A

AGR-2 Compact Cross-section Montages

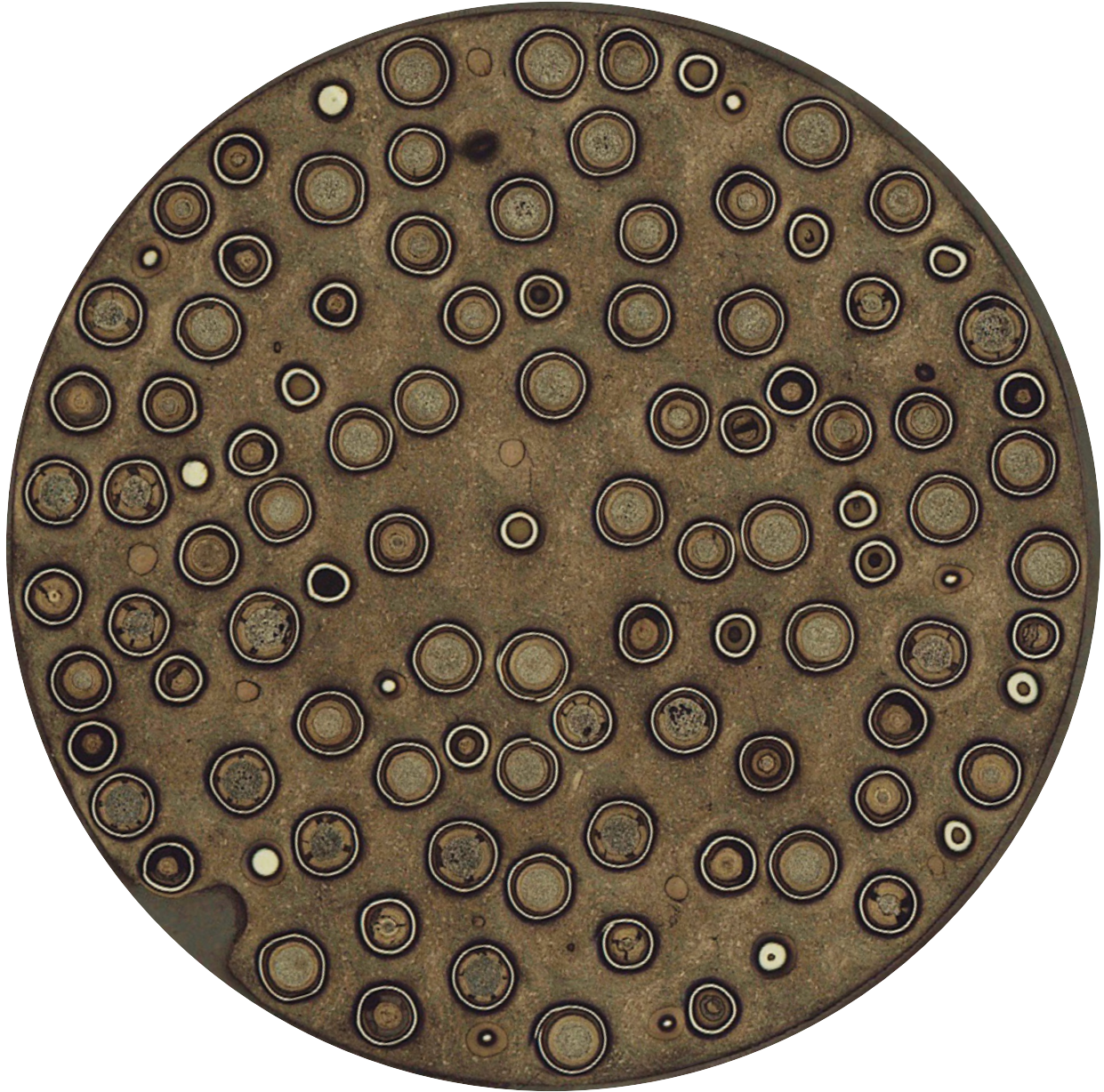


Figure A-1. UCO Compact 2-1-3 center, MNT 67X micrograph montage.

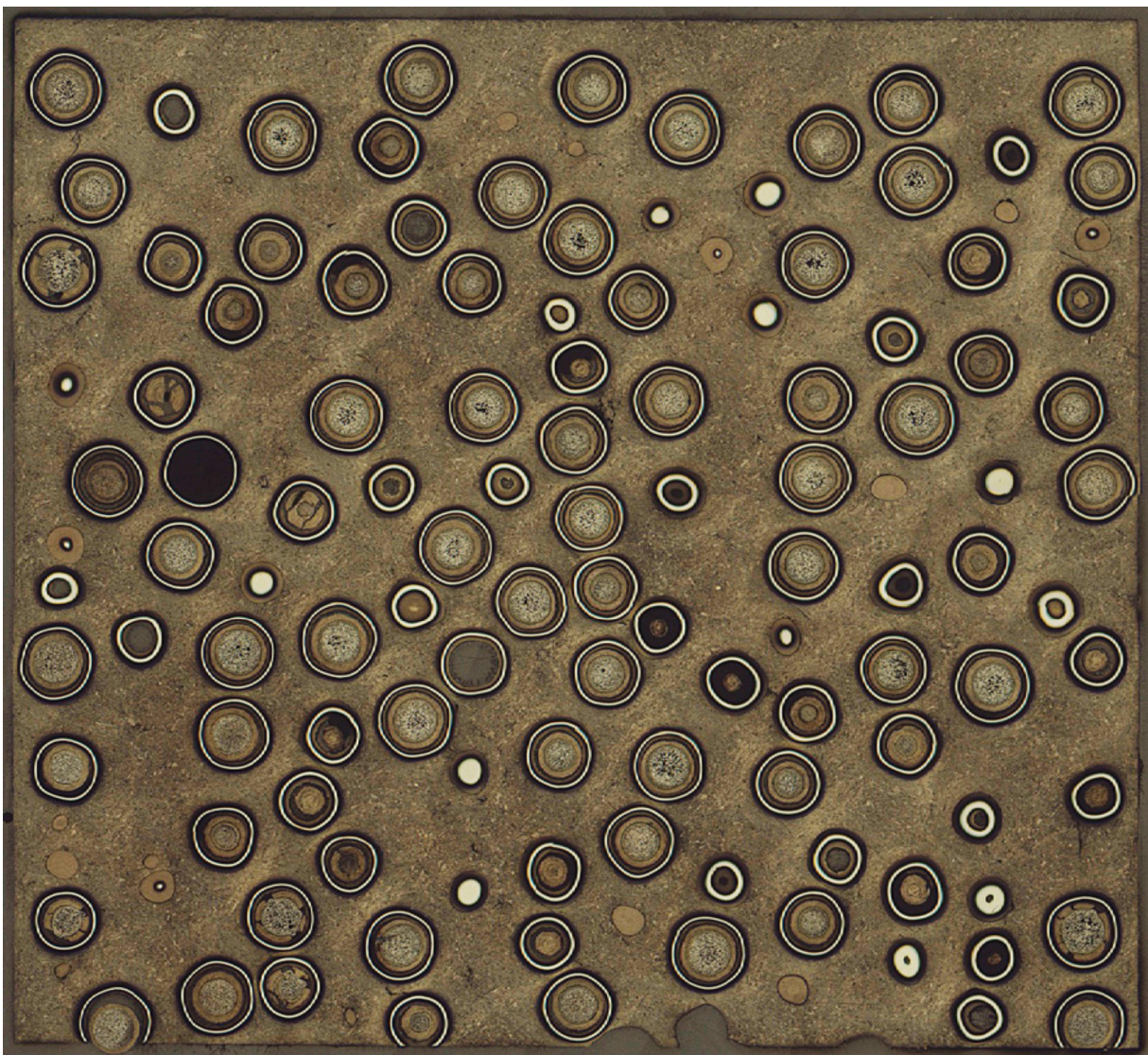


Figure A-2. UCO Compact 2-1-3 top, MNT 69X micrograph montage.



Figure A-3. UCO Compact 2-1-3 bottom, MNT 68X micrograph montage.

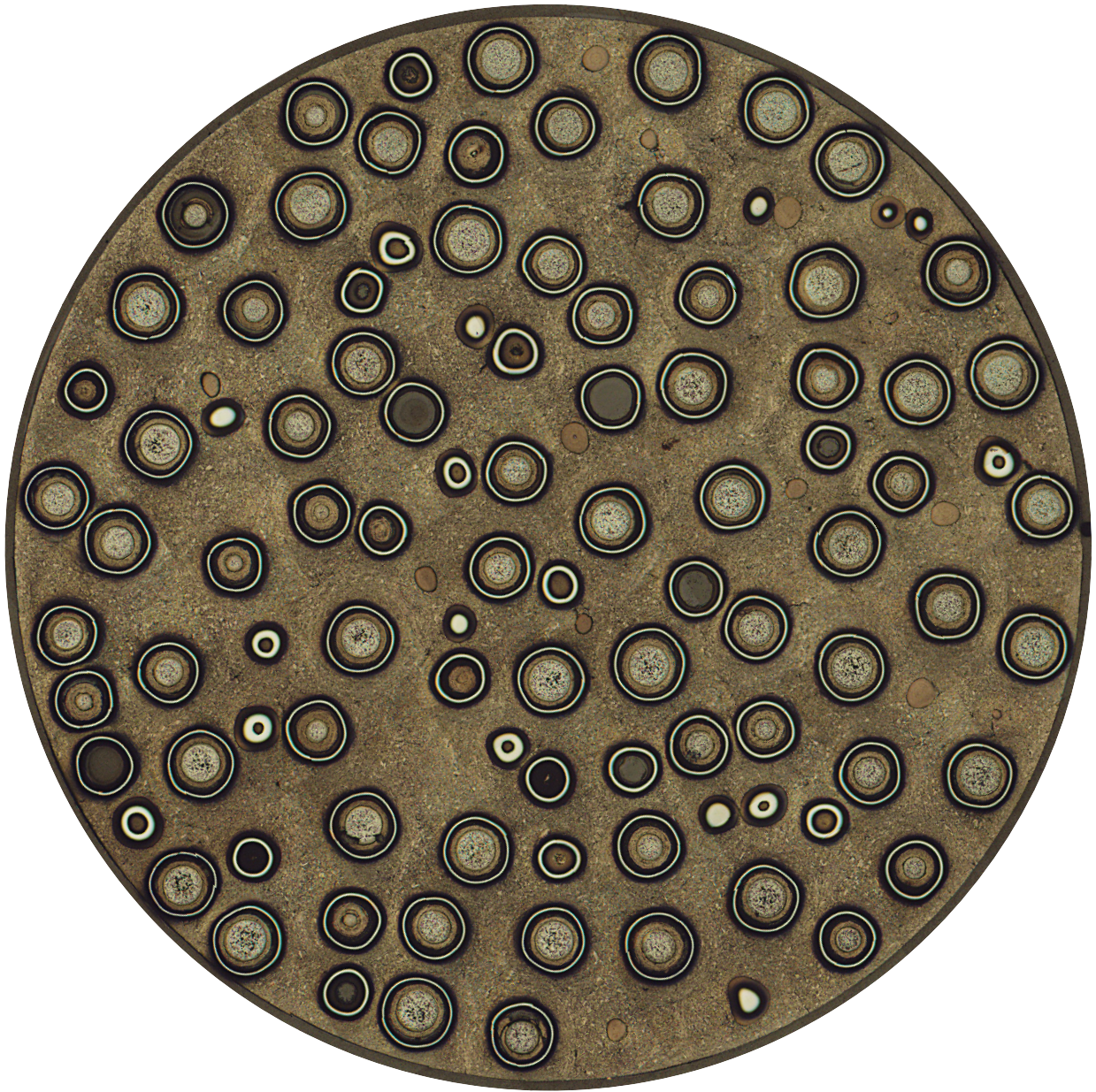


Figure A-4. UCO Compact 2-4-3 middle, MNT 58X micrograph montage.

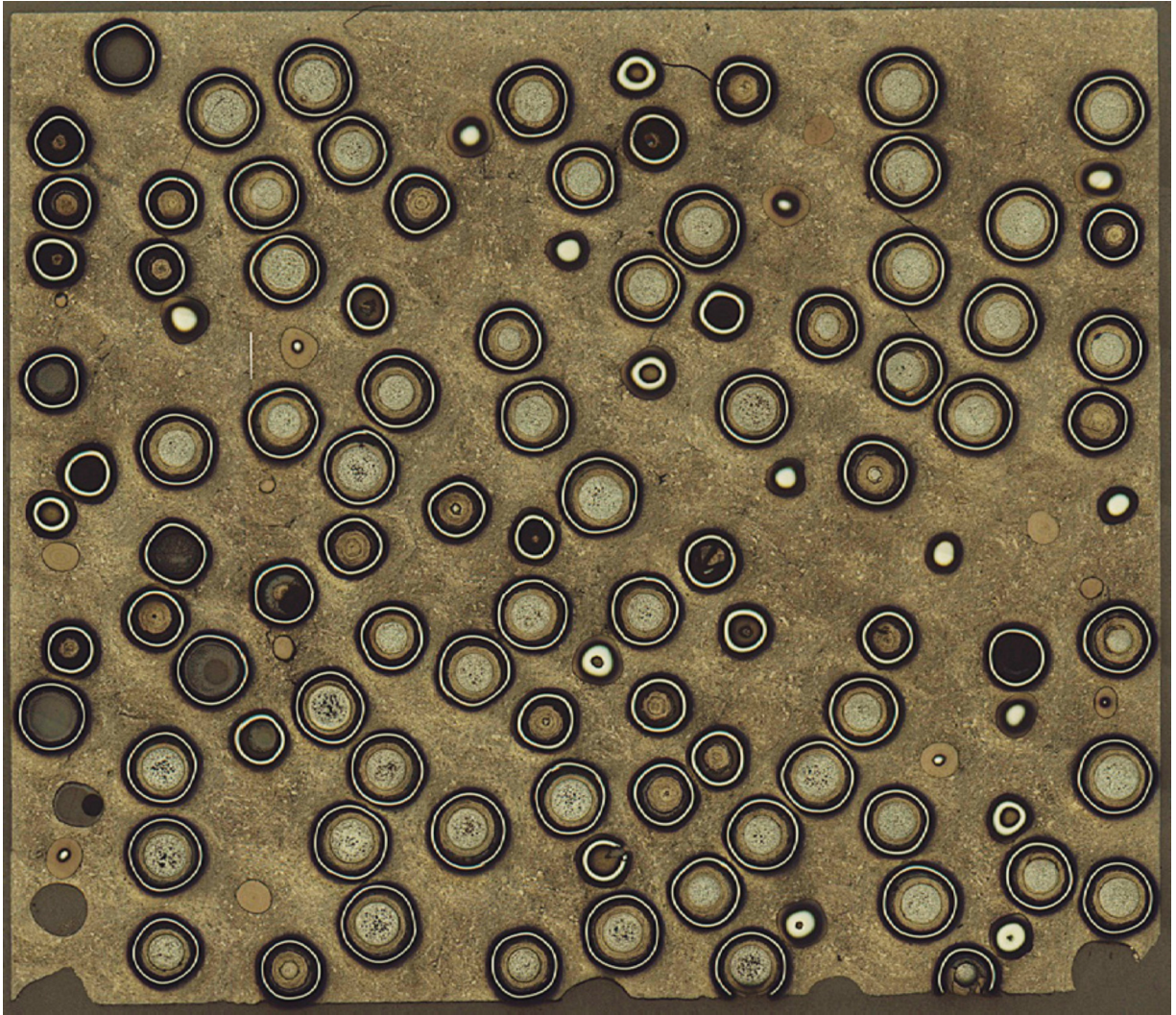


Figure A-5. UCO Compact 2-4-3 top, MNT 60X micrograph montage.

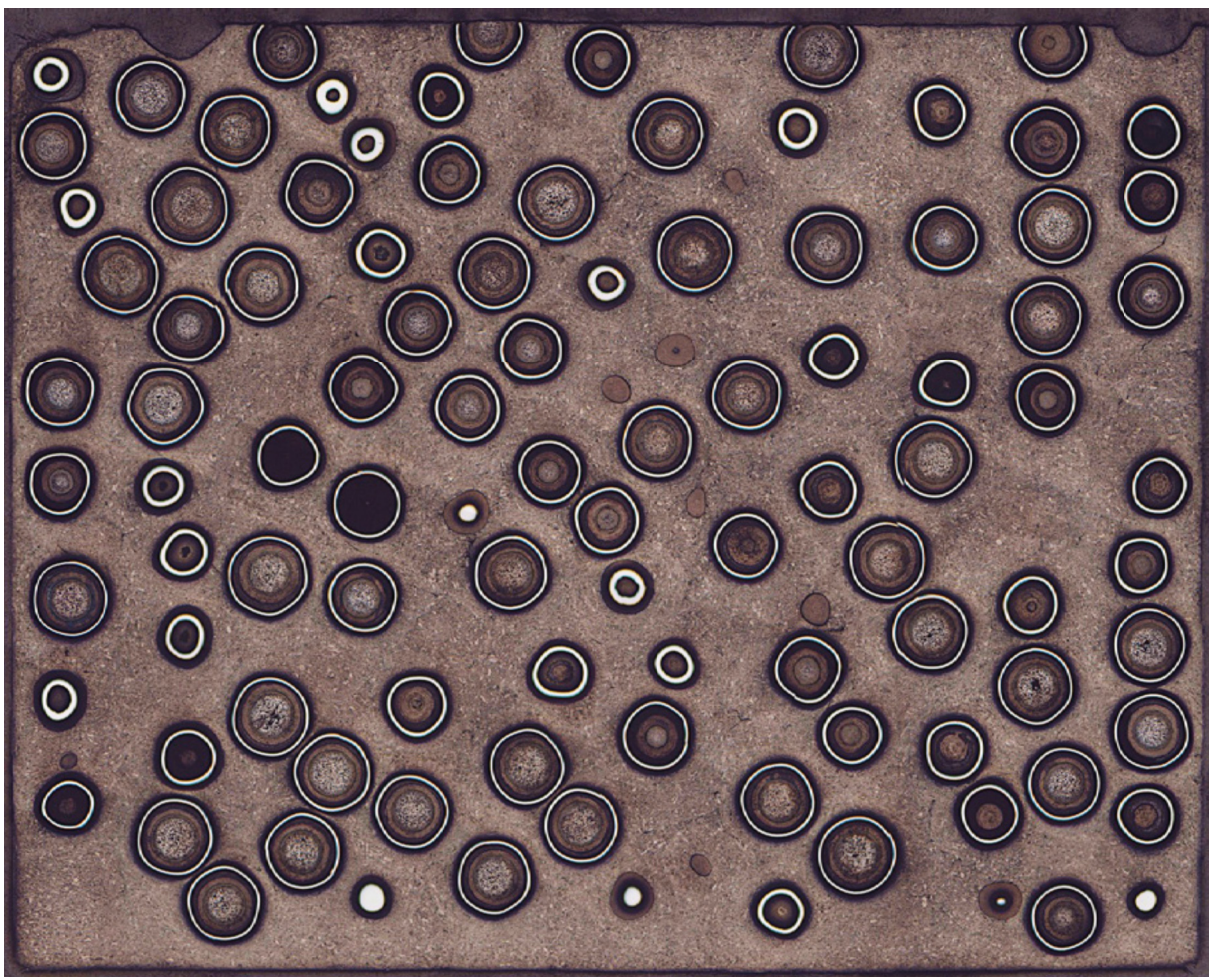


Figure A-6. UCO Compact 2-4-3 bottom, MNT 59X micrograph montage.



Figure A-7. UO₂ Compact 3-2-3 middle, MNT 61X micrograph montage.

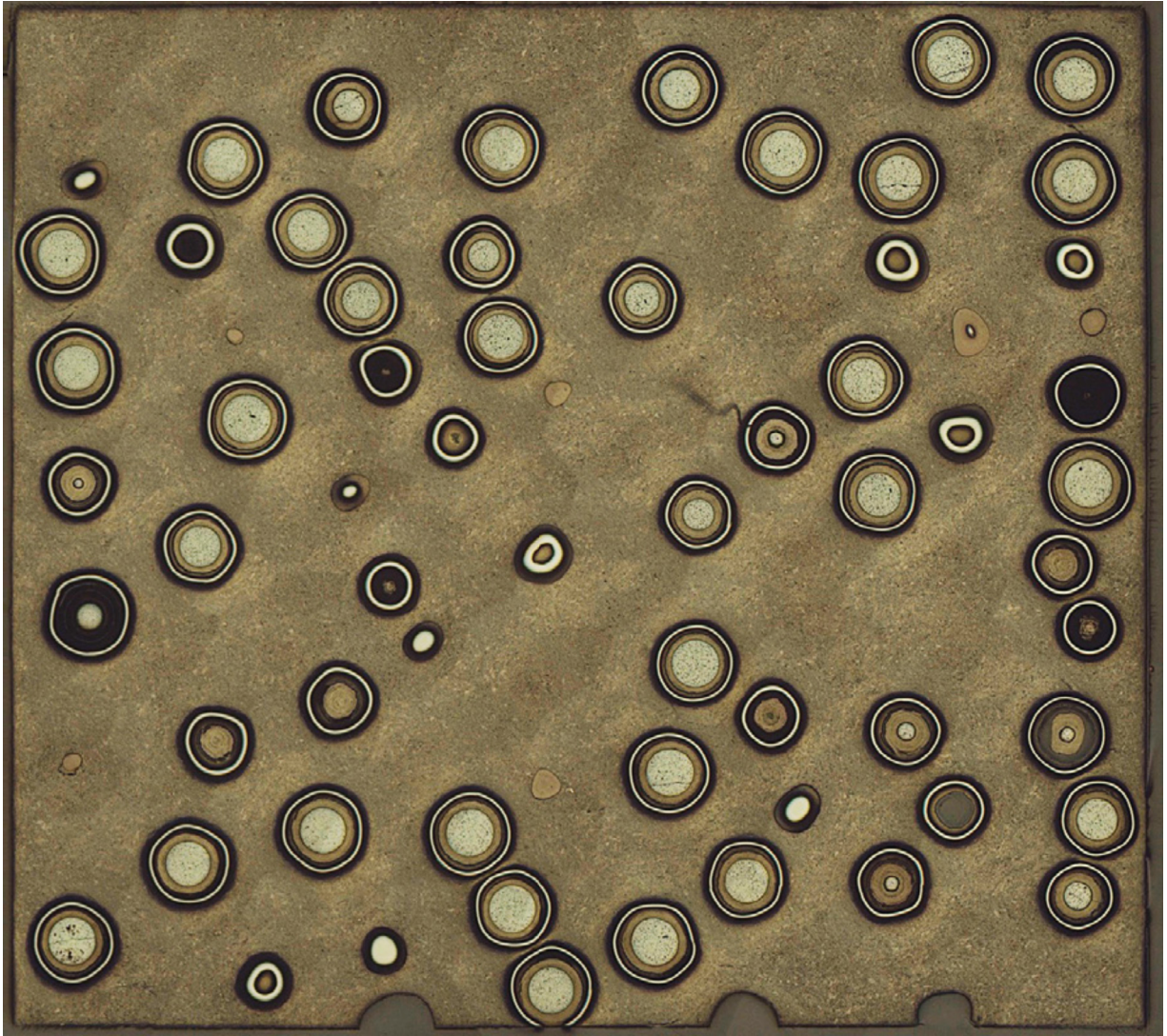


Figure A-8. UO_2 Compact 3-2-3 top, MNT 63X micrograph montage.

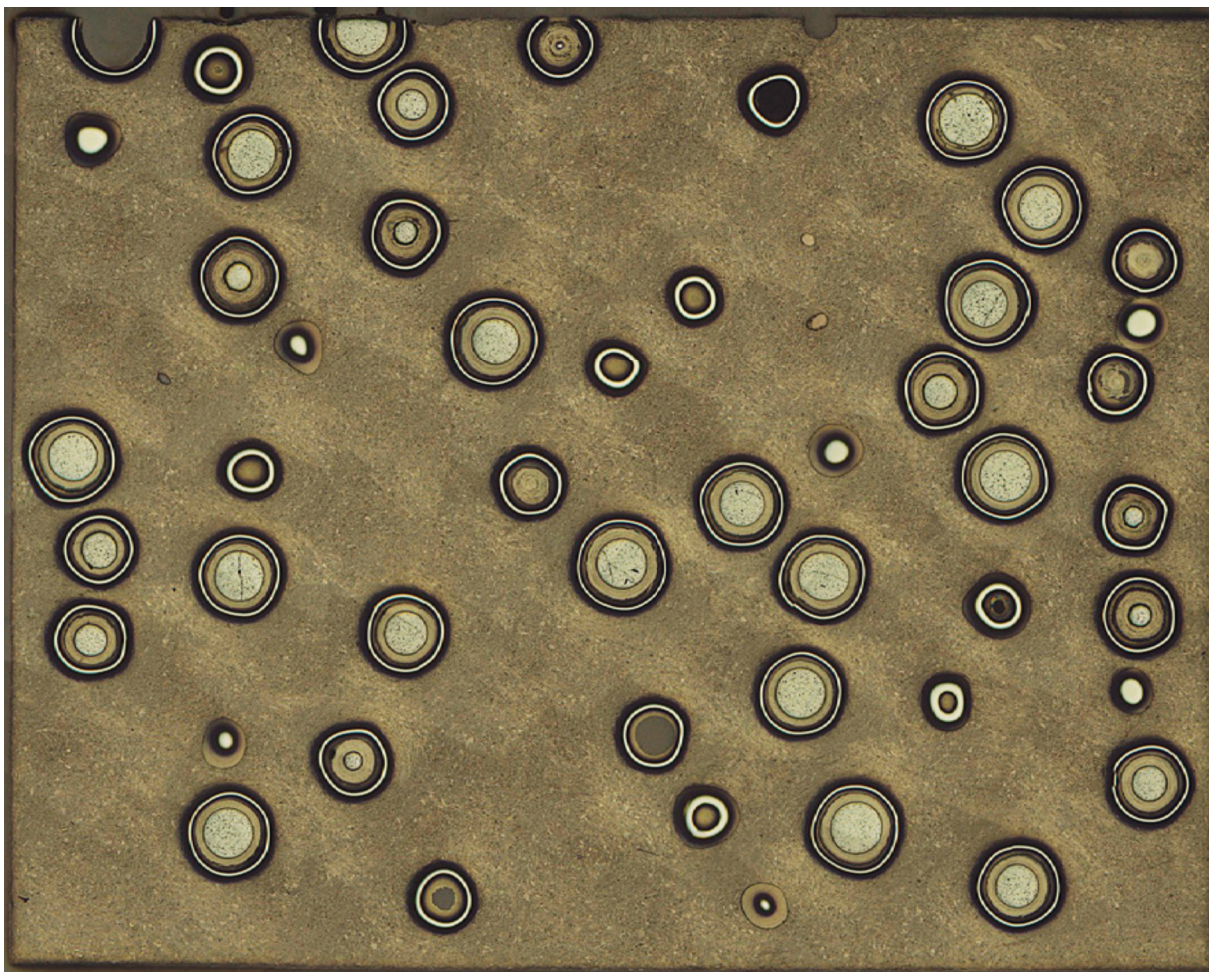


Figure A-9. UO_2 Compact 3-2-3 bottom, MNT 62X micrograph montage.



Figure A-10. UCO Compact 5-1-3 middle, MNT 64X micrograph montage.

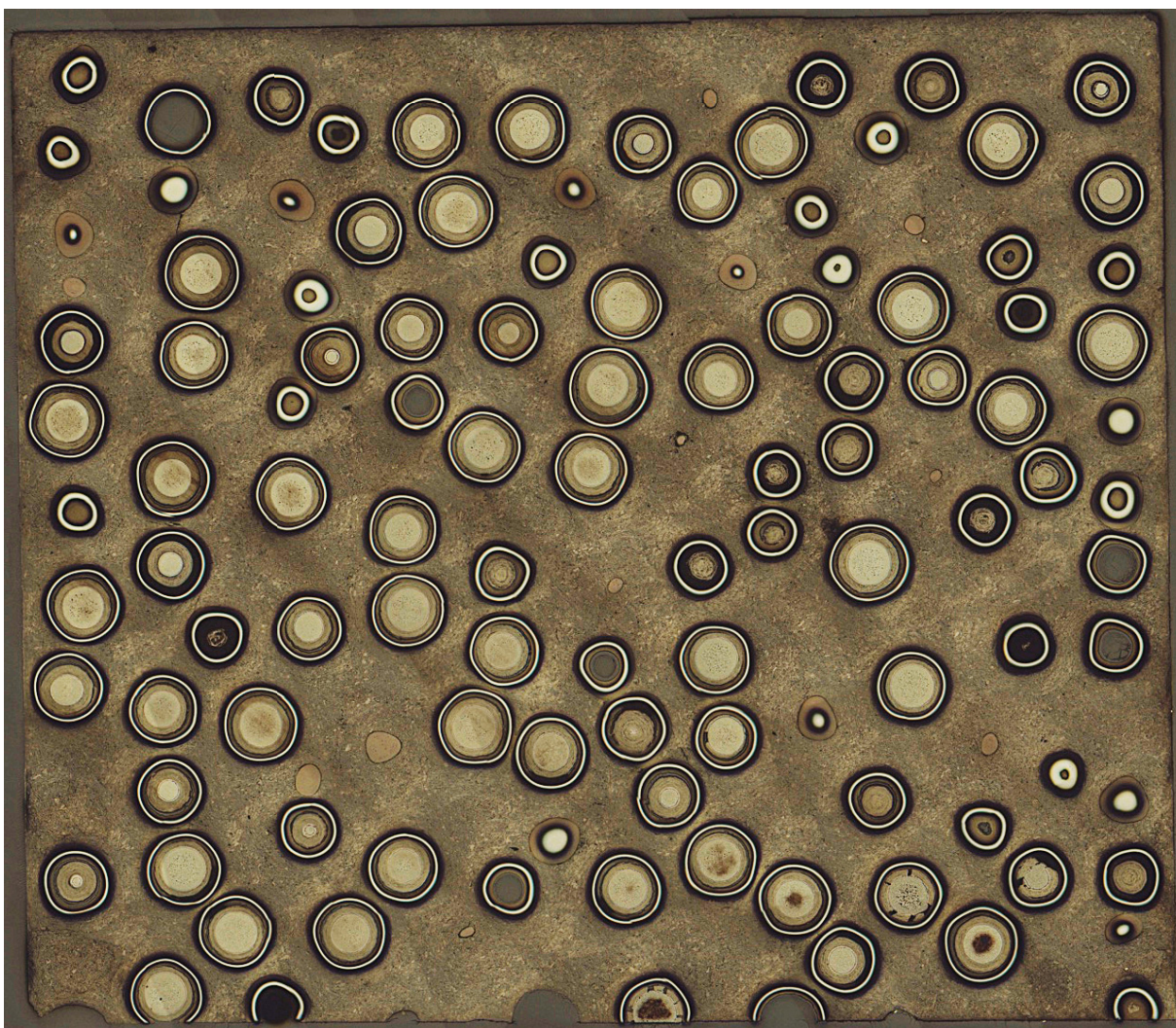


Figure A-11. UCO Compact 5-1-3 top, MNT 66X micrograph montage.

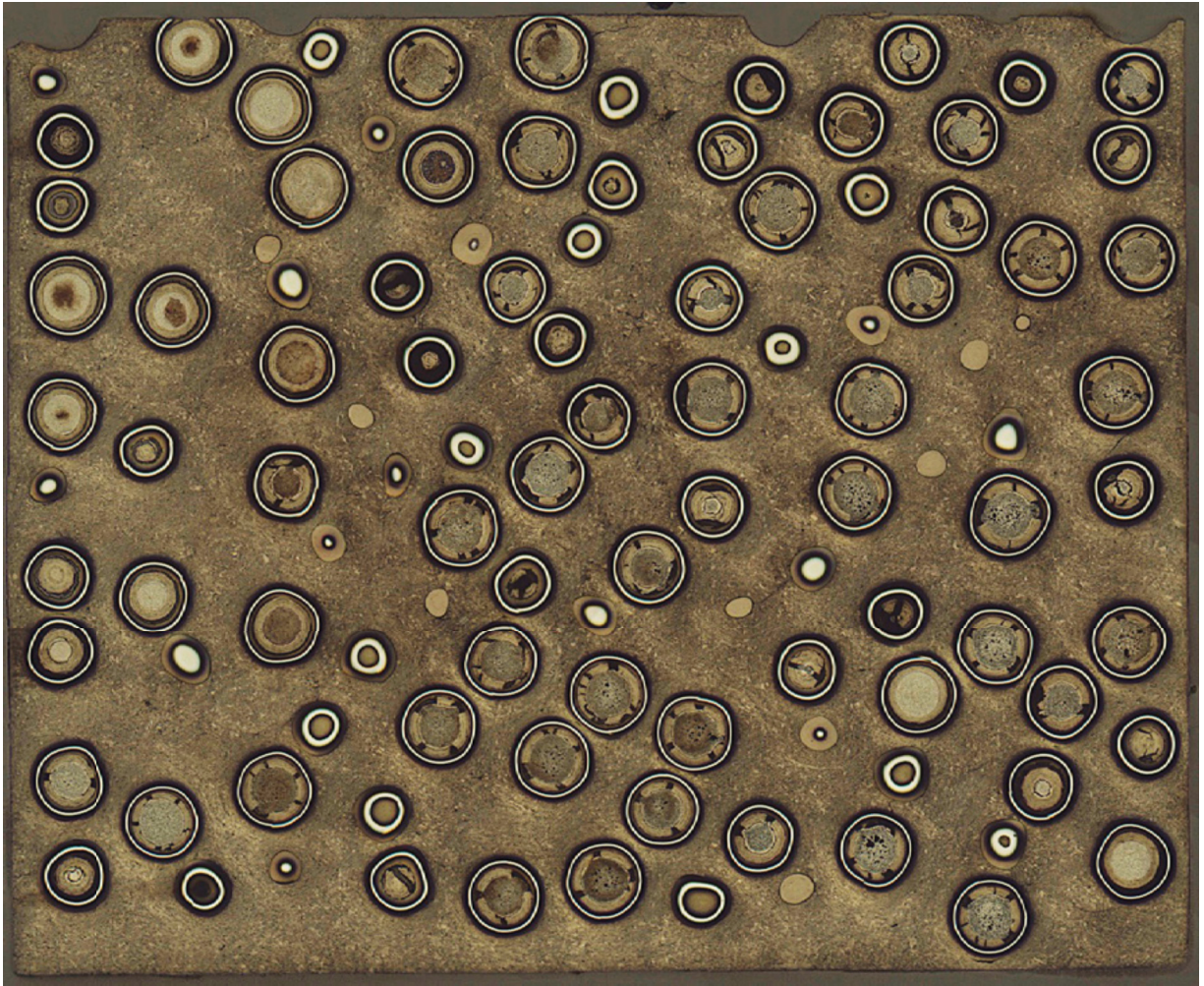


Figure A-12. UCO Compact 5-1-3 bottom, MNT 65X micrograph montage.